Development and testing of Polar Weather Research and Forecasting model: 2. Arctic Ocean

David H. Bromwich,[1,2] Keith M. Hines,[1] and Le-Sheng Bai[1]

[1] A version of the state-of-the-art Weather Research and Forecasting model (WRF) has been developed for polar applications. The model known as "Polar WRF" is tested over the Arctic Ocean with a western Arctic grid using 25-km resolution. The model is based upon WRF version 2.2, with improvements to the Noah land surface model and the snowpack treatment. The ocean surface treatment is modified to include fractional sea ice. Simulations consist of a series of 48-h integrations initialized daily at 0000 UTC. The initial 24 h are taken as model spin-up time for the atmospheric hydrology and boundary layer processes. Arctic conditions are simulated for the selected months: January 1998, June 1998, and August 1998 representing midwinter, early summer, and late summer conditions, respectively, from the Surface Heat Budget of the Arctic (SHEBA) study. The albedo of sea ice is specified as a function of time and latitude for June and as a function of time for August. Simulation results are compared with observations of the drifting ice station SHEBA in the Arctic ice pack. Polar WRF simulations show good agreement with observations for all three months. Some differences between the simulations and observation occur owing to apparent errors in the synoptic forecasts and the representation of clouds. Nevertheless, the biases in the simulated fields appear to be small, and Polar WRF appears to be a very good tool for studies of Arctic Ocean meteorology.

Citation: Bromwich, D. H., K. M. Hines, and L.-S. Bai (2009), Development and testing of Polar Weather Research and Forecasting model: 2. Arctic Ocean, *J. Geophys. Res.*, *114*, D08122, doi:10.1029/2008JD010300.

1. Introduction

[2] It is well known in the scientific community that the Arctic region is especially sensitive to climate change, with the sea-ice albedo feedback playing a critical factor [*Curry et al.*, 2001; *McBean et al.*, 2004; *ACIA*, 2005]. Moreover, very recent observations demonstrate that Arctic sea ice is decreasing much more rapidly than projected [e.g., *Stroeve et al.*, 2007]. Therefore, it is critical to have accurate numerical tools to understand and predict the physical processes at work in the Arctic environment. Unfortunately, the Arctic is an especially challenging region for numerical modeling, though several recent observational studies have provided invaluable insight [e.g., *Curry*, 2001; *Verlinde et al.*, 2007]. Several other studies have addressed the thermodynamics and rheology of Arctic sea ice with prognostic models [e.g., *Huwald et al.*, 2005; *Zhang and Rothrock*, 2005; *DeWeaver and Bitz*, 2006]. The current study, however, will consider numerical simulations of the Arctic atmosphere, including the boundary layer adjacent to sea ice.

[3] In a recent work, *Hines and Bromwich* [2008], referred to as HB, introduced a version of the Weather Research and Forecasting model (WRF) known as Polar WRF. The new model represents the next generation to continue the research and operational applications of the polar version [e.g., *Bromwich et al.*, 2001] of the Pennsylvania State University–National Center for Atmospheric Research (PSU–NCAR) fifth-generation Mesoscale Model (MM5) [*Grell et al.*, 1994]. Previously, Polar MM5 was optimized for the polar regions at Ohio State University in collaboration with the Mesoscale and Microscale Meteorology (MMM) Division at NCAR, and implemented into the MM5 community modeling system managed by NCAR. Polar MM5 demonstrated a high level of performance for both Arctic and Antarctic regions [e.g., *Bromwich et al.*, 2001; *Cassano et al.*, 2001; *Powers et al.*, 2003]. The model WRF has significant advantages over MM5 including more efficient software, energy conservation and new physical parameterizations [e.g., *Skamarock et al.*, 2005]. Polar WRF simulations over a Greenland–North Atlantic grid by HB demonstrate a forecast skill over the Greenland Ice Sheet at least as good as that of Polar MM5, along with an improved surface energy balance. Furthermore, Polar WRF replaced Polar MM5 during June 2008 as the base model for the high-resolution numerical forecasts of Antarctic Mesoscale Prediction System (AMPS) [*Bromwich et al.*, 2003; *Powers et al.*, 2003] in support of operational and logistic needs of the United States Antarctic Program. Extensive testing of

---

[1]Polar Meteorology Group, Byrd Polar Research Center, Ohio State University, Columbus, Ohio, USA.
[2]Atmospheric Sciences Program, Department of Geography, Ohio State University, Columbus, Ohio, USA.

Polar WRF in the AMPS framework is being performed [e.g., *Powers*, 2007].

[4] In the current paper, Polar WRF is now evaluated over the Arctic Ocean. We select test periods from the Surface Heat Budget of the Arctic Ocean (SHEBA) program during 1997–1998 when detailed measurements were available from the drifting Ice Station SHEBA [*Perovich et al.*, 1999; *Uttal et al.*, 2002]. Cloud observations were especially enhanced for the First ISCCP Regional Experiment (FIRE) Arctic Clouds Experiment during April–July 1998 [*Curry et al.*, 2000]. The SHEBA period has previously been used for model evaluation via the Arctic Regional Climate Model Intercomparison Project (ARCMIP) developed by *Curry and Lynch* [2002] to improve climate modeling of the Arctic [*Tjernström et al.*, 2005]. The Arctic Ocean surface during SHEBA represents one of three key land surface types for development and testing of Polar WRF. The other two include ice sheet surfaces previously evaluated with simulations by HB, and Arctic land surfaces to be evaluated in simulations via a forthcoming paper.

[5] The current modeling study responds to the call for extensive, interdisciplinary, multiscale studies of high northern latitude climate through the Study of Environmental Arctic Change (SEARCH) [*Overland et al.*, 2003]. To integrate observations and modeling efforts into a comprehensive picture of the climate and synoptic meteorology of the Arctic, SEARCH includes the development of a multiyear Arctic System Reanalysis (ASR, http://polarmet.mps.ohio-state.edu/PolarMet/ASR.html) from all available remote sensing and in situ data. The development of Polar WRF is partly in response to the need for an Arctic-friendly atmospheric numerical model with state-of-the-art dynamics and physical packages that permit WRF to describe polar specific processes. Advanced data assimilation capabilities for WRF being developed at NCAR are another key prerequisite for the ASR [e.g., *Cucurull et al.*, 2006; *Xiao et al.*, 2008].

2. Polar WRF

[6] Testing of the next generation WRF model (http://wrf-model.org) for polar applications began with the Greenland-area simulations of HB. The Advanced Research WRF (ARW) is a modular, nonhydrostatic model designed for both research and operational applications [*Skamarock et al.*, 2005]. The development and evaluation of Polar MM5 had been detailed through a series of publications [*Bromwich et al.*, 2001; *Cassano et al.*, 2001; *Guo et al.*, 2003; *Monaghan et al.*, 2005]. Analogous to the development of Polar MM5, evaluations and improvements are needed for the boundary layer parameterization, cloud physics and cloud-radiative processes, snow surface physics and sea-ice treatment of Polar WRF. The Greenland-area simulations used a variety of WRF's physical parameterization options and identified a set of parameterizations favorable for polar conditions.

[7] The Polar WRF simulations described here utilize modifications to version 2.2 of the ARW. The simulations have the same 28 terrain-following sigma layers between the Earth's surface and the model top at 10 hPa as in HB. The top is set at a high level for better treatment of upward propagating gravity waves generated by topography [e.g.,

Guo et al., 2003; *Bromwich et al.*, 2005a]. Highest vertical resolution is in the boundary layer with the lowest 10 layers over the Arctic Ocean centered at approximately 14, 42, 75, 118, 171, 238, 325, 433, 561, and 748 m, respectively, above the surface. The time step is 120 s for January runs. A shorter time step, 60 s, is required and selected for numerical stability of the June and August runs. Furthermore, subgrid-scale cumulus is parameterized with the *Grell and Devenyi* [2002] ensemble scheme, as the earlier Grell scheme gave good results for Polar MM5 simulations of summer climate near the Laurentide ice sheet [*Bromwich et al.*, 2005b].

[8] For cloud physics, Polar WRF has added a version of the *Morrison et al.* [2005] bulk microphysics scheme that is two-moment for cloud ice, cloud liquid, rain, snow and graupel. In HB, the WRF single-moment five-class microphysics scheme was employed. The new scheme is more realistic and is being developed and tested for the Arctic [e.g., *Morrison et al.*, 2008]. The scheme predicts both number concentration and mixing ratio of cloud species. It was tested within Polar MM5 by *Morrison and Pinto* [2005, 2006] for Arctic mixed-phase clouds during May 1998 and shown to reasonably simulate cloud persistence and microphysical characteristics.

[9] The simulations over Greenland by HB identified the following parameterizations now used for the SHEBA simulations. For long-wave radiation, the Rapid Radiative Transfer Model (RRTM) [*Mlawer et al.*, 1997] is selected. The RRTM alleviates the deficit in downward long-wave radiation for clear-sky conditions present in many earlier radiation schemes [e.g., *Pinto et al.*, 1997]. Short-wave radiation is represented by the Goddard scheme with 11 spectral bands that accounts for both diffuse and direct solar radiation [*Chou and Suarez*, 1999]. For the planetary boundary layer, we employ the Mellor-Yamada-Janjić (MYJ) scheme, run in conjunction with the Eta surface layer scheme also based on similarity theory [*Janjić*, 2002]. The land surface is treated with the four-layer Noah land surface model (LSM) [*Chen and Dudhia*, 2001; *Skamarock et al.*, 2005] with the polar updates from HB, including modifications to the surface energy balance solution and the upward long-wave flux. The surface temperature, T_s, over frozen surfaces is obtained by an iterative solution to the surface energy balance,

$$0 = \varepsilon\big[L(\downarrow) - \sigma T_s^4\big] + [1 - \alpha]S(\downarrow) - H_s - L_s + G + Q, \quad (1)$$

where ε is surface emissivity, $L(\downarrow)$ is downward long-wave radiation, σ is the Stephan-Boltzman constant, α is surface albedo, $S(\downarrow)$ is downward short-wave radiation, H_s is the sensible heat flux, L_s is the latent heat flux, and G is the ground heat flux. Q represents other diabatic processes, as in HB. In the numerical solution of (1), L_s and Q are calculated first, then iterative steps adjust H_s and G with T_s.

[10] The evapotranspiration in the Noah LSM has been updated as in HB. Previously, evapotranspiration was obtained from surface energy balance considerations through the Penman-Monteith equation. Evaporation from liquid surfaces was considered, but not sublimation from frozen surfaces. The modified Noah now has a modified
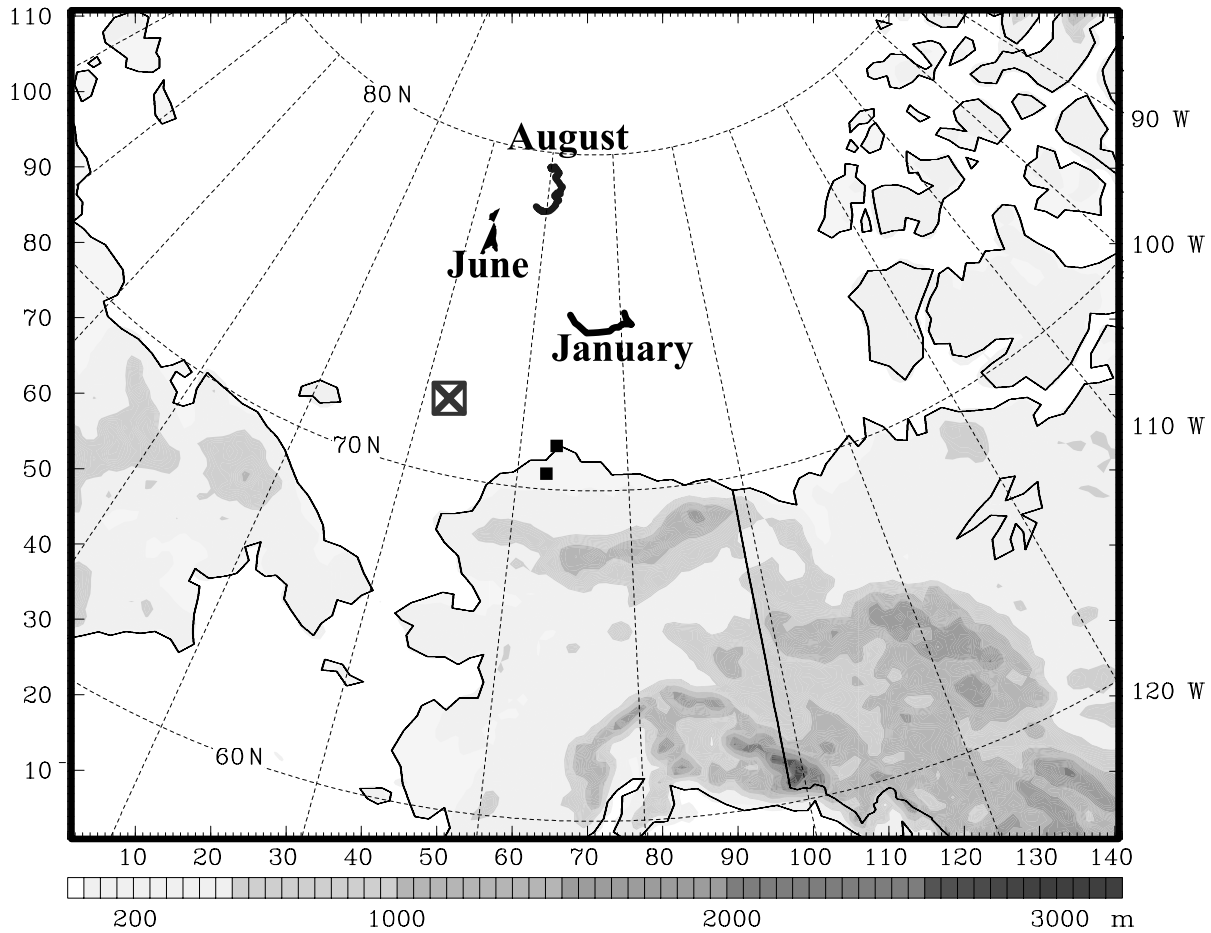
Figure 1. Domain for the Polar WRF simulations. Marks in the Arctic Ocean show the location of Ice Station SHEBA during January, June, and August 1998. The cross inside the square shows the location of the grid point at 72.28°N, 167.65°W. Squares show Atmospheric Radiation Measurement stations Barrow and Atqasuk.

Penman-Monteith equation that includes sublimation, analogous to work of *Mahrt and Vickers* [2005]. As in HB, the heat transfer, thermal conductivity, heat capacity and density are modified for ice sheet surfaces to more closely match those of Polar MM5.

[11] A new feature recently added to Polar WRF for these simulations is the treatment of fractional sea ice with different surface conditions for the ice and open-water portions of sea-ice grid points. First, the surface atmospheric-layer component of WRF's boundary layer treatment is called separately for the ice and open-water fractions of a grid box. The surface exchange coefficients and surface fluxes are stored for the fractions. Using the surface exchange coefficients for the ice fraction, the next step is a call to the LSM routine only for the ice fraction, and new surface fluxes and new surface-level variables are computed there. Over open ocean, WRF does not invoke the LSM, and surface fluxes are calculated by the surface layer component of the boundary layer parameterization [*Skamarock et al.*, 2005]. Model surface parameters that differ between the ice and open-water fractions include surface roughness and albedo. Through the mosaic method, the surface fluxes and surface variables in a grid box are areally averaged with contributions from the ice and water fractions [*Avissar and Pielke*, 1989; *Vihma*, 1995],

$$x = x_i A_i + x_w (1 - A_i), \qquad (2)$$

where x is a quantity, the subscripts i and w refer to the ice and open-water components, respectively, and A_i is the fractional area of sea ice.

[12] Sea-ice fraction and open-water sea surface temperature are prescribed values that do not vary during a 48-h simulation for WRF version 2.2. The open-water sea surface temperature for sea ice grid points is obtained from the model input data sets and is not necessarily upper bounded at its freezing point. Beneath the prognostic subsurface layers, the Noah LSM assigns the fixed temperature 271.16 K where there is sea ice. The horizontal distribution of sea-ice thickness may also strongly influence surface fluxes for pack ice [e.g., *Ebert and Curry*, 1993; *Overland et al.*, 2000], however, the inclusion of ice thickness variation is beyond the scope of this paper. The fractional sea-ice treatment is modular and can be employed with other land surface models.
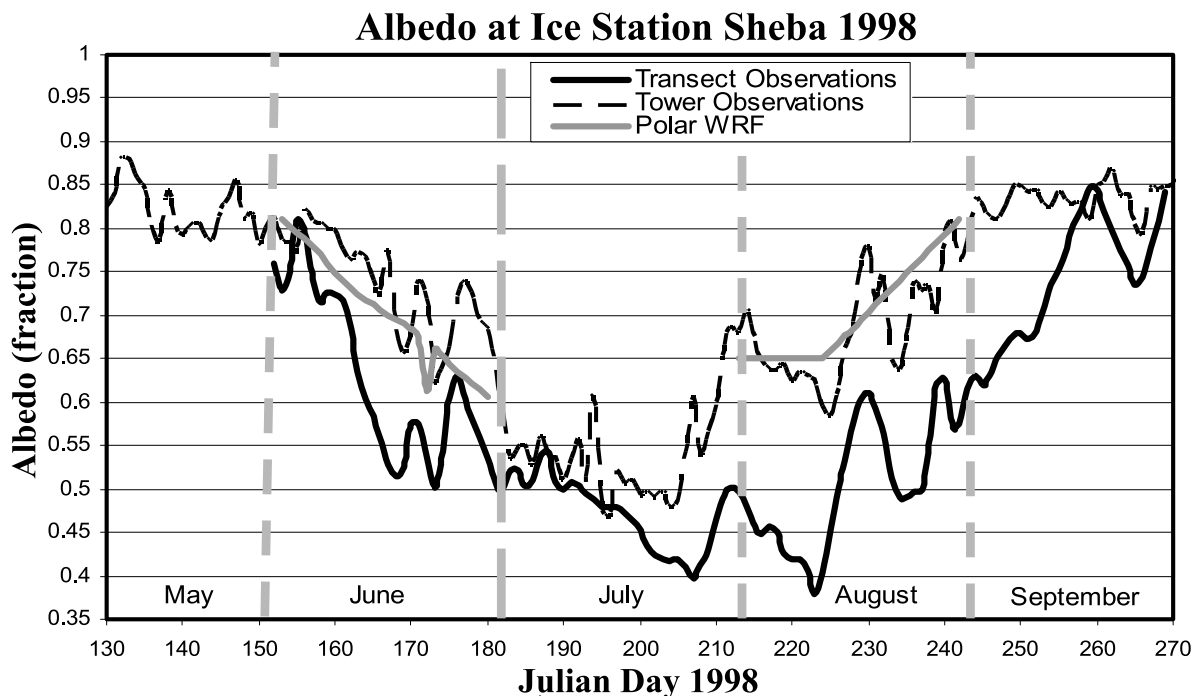
Albedo at Ice Station Sheba 1998

Figure 2. Albedo as a function of Julian day for 1998. Thick solid line shows the area-average albedo from transect observations near Ice Station SHEBA. The thin line shows the locally measured albedo at the SHEBA tower. The thick gray line is the Polar WRF value interpolated to the SHEBA track.

[13] For Greenland, and analogously for Antarctica, the majority of the ice sheet area remains highly reflective over the annual cycle. Observations suggest some variability due to location and time [e.g., *Stroeve et al.*, 2001]; nevertheless, the value, 0.80, employed by HB appears to be a good representative value for ice sheet surfaces. Sea ice albedo, however, has significant variations due to a number of factors. Arctic sea ice, for example, has a strong seasonal cycle with large changes not just in areal coverage, but also in important surface characteristics [*Perovich et al.*, 2002b; *Persson et al.*, 2002]. *Perovich et al.* [2002a, 2007] demonstrate that surface albedo strongly depends on the seasonal freeze-thaw cycle. A prognostic regional system model with atmospheric, sea ice and ocean components would be required to capture the full range of surface conditions for Arctic sea ice. For this research study, we have selected a methodology with prescribed sea-ice surface conditions designed to include first-order seasonal variations for the Arctic Ocean. Users of Polar WRF will need to specify sea ice albedo appropriate for their applications. A detailed discussion of the sea-ice albedo and its treatment for the Polar WRF simulations is included in Appendix A.

3. Arctic Domain

[14] The Polar WRF simulations shown here encompass a western Arctic domain extending 3500 km east to west and 2750 km north to south. The Lambert conformal grid is centered at 72°N, 153°W with 25 km horizontal grid spacing (Figure 1). The domain is similar to the ARCMIP grid with twice the spatial resolution. North of Alaska, the

locations of the drifting Ice Station SHEBA during January 1998, June 1998 and August 1998 are shown in Figure 1. The ice camp drifted over a latitude range from 75°N to 81°N and a longitude range from 140°W to 170°W during the October 1997 to October 1998 observational study [*Perovich et al.*, 2007]. For evaluation, WRF results are bilinearly interpolated from the four nearest grid points to concurrent locations of the drifting ice station for comparison to the SHEBA observed surface data [*Persson et al.*, 2002].

[15] The SHEBA observations include latitude, longitude, surface pressure, temperature, velocity, humidity, precipitation, turbulent fluxes, and radiative fluxes [*Persson et al.*, 2002]. Quality-controlled values can found at ftp://ftp.etl. noaa.gov/user/opersson/sheba/. Some observed values are taken at the surface. Other values are measured at five levels on the 20-m Atmospheric Surface Flux Group (ASFG) flux tower, averaged over 1 hour, and interpolated to 2.5 m and 10 m above the surface [*Persson et al.*, 2002]. Measurements of broadband incoming and outgoing radiative fluxes were made on a shorter mast situated 30 m from the flux tower. In addition, cloud fraction was reported by the ship's crew every 6 h while measurements of cloud fraction and other cloud parameters are available from a cloud radar, depolarization lidar, and microwave radiometer [*Shupe et al.*, 2005]. Manual observations of snow depth and albedo were made near solar noon at least weekly from April 1998 onward and every other day from June to August every 2.5 m along a 200-m transect over different surface conditions [*Perovich et al.*, 2002b; *Persson et al.*, 2002]. Aerial photography was also employed to study the surface con-
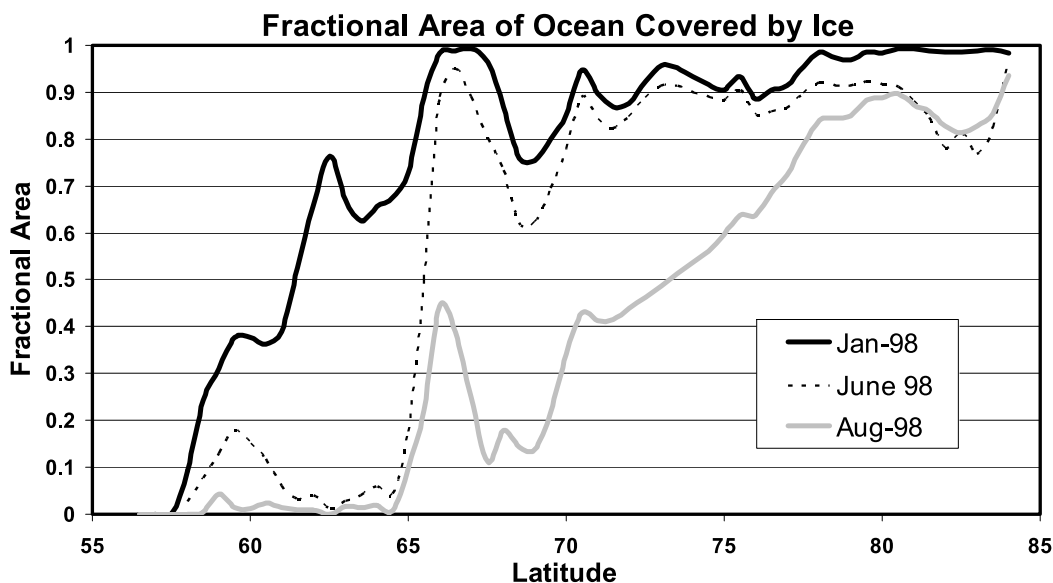
Figure 3. Fractional area of the ocean covered by ice as a function of latitude within the model domain for the January, June, and August 1998 simulations. Special Sensor Microwave Imager (SSM/I) retrievals of sea-ice fraction are supplied by the National Snow and Ice Data Center (NSIDC).

ditions influencing the radiative balance [*Perovich et al.*, 2002b]. Figure 2 shows time variation of observed albedo from tower and transect observations.

[16] For the Polar WRF simulations of the Arctic domain, specified initial and boundary conditions for the atmospheric fields are taken from European Centre for Medium-Range Weather Forecasts (ECMWF) 40-year reanalysis (ERA-40) [*Uppala et al.*, 2005] fields available every 6 h at 2.5° × 2.5° resolution. The SHEBA observations were assimilated by ECMWF into the ERA-40 fields and, therefore, impact the initial conditions for mesoscale simulations performed here. The initial conditions should be high quality near SHEBA. *Bromwich and Wang* [2005] and *Bromwich et al.* [2007] evaluated the performance of ERA-40 in the Arctic. Bromwich and Wang compared ERA-40 fields against two independent data sets and found that geopotential height, temperature and humidity demonstrate close agreement with rawinsonde observations from the periphery of the Arctic Ocean. Spring tropospheric wind measurements from the Leadex project in the Beaufort Sea, which were not assimilated into ERA-40, showed close agreement with ERA-40 values. Bromwich et al. showed that an Arctic cold bias was present for earlier ERA-40 years; however, the bias was not found for 1998 onward. Thus the 1998 SHEBA months are not impacted. As surface pressure was not available on the 2.5° × 2.5° grid, the ERA-40 data are supplemented by surface pressure fields every 12 h from the ECMWF Tropical Ocean Global Atmosphere (TOGA) operational analyses. Additionally, sea surface temperature is obtained from the National Centers for Environmental Prediction (NCEP) analyses.

[17] The fractional sea-ice coverage for the ocean grid points is prescribed from daily sea-ice fraction determined from the bootstrap algorithm for dual-polarized and multi-frequency Special Sensor Microwave/Imager (SSM/I) microwave radiometer measurements, available from the

National Snow and Ice Data Center (NSIDC) at 25-km resolution [*Comiso*, 2002]. *Valkonen et al.* [2008] find the best results in their Antarctic simulations with Polar MM5 when the prescribed sea-ice fraction is obtained from the bootstrap algorithm. Figure 3 displays the fraction of the ocean surface in Figure 1 covered by ice as a function of latitude for the months of January, June and August 1998. Significantly more sea ice is present during January for ocean surfaces south of 65°N. The fraction of open water over the Arctic Ocean (essentially latitudes north of 70°N) is much larger during August than during January or June. The August sea-ice fraction for the domain is displayed in Figure 4. Within a few hundred kilometers of the Alaskan coast, sea-ice fraction is generally less than 80% for this month. Between northern Alaska and Siberia, the Chukchi Sea is primarily ice free. A region of reduced sea-ice fraction also extends northward near 160°W, including near the location of SHEBA. On the other hand, the Arctic Ocean, including near SHEBA, is heavily ice covered during January and June, as suggested by Figure 3. In contrast to the August values shown in Figure 4, during June the region of greater than 50% ice coverage extends southward to the Bering Strait. During January, a narrow wedge of greater than 50% sea-ice coverage extends south of the Bering Strait (not shown).

[18] Initial sea-ice temperature for the four constant thickness Noah LSM layers is interpolated from the ERA-40 ice temperature. The ERA-40 subsurface temperature is provided from the layers at 0–0.07 m, 0.07–0.28 m, 0.28–1.0 m, 1.0–2.55 m. For land grid points, initial soil temperature is also interpolated from ERA-40 values.

[19] Spin-up of the Polar WRF simulated Arctic fields, especially those of the boundary layer and atmospheric hydrology, is allowed to occur over a full day. The output prior to hour 24 is discarded for each individual simulation (beginning at 0000 UTC each day), and hour 24–45 of the
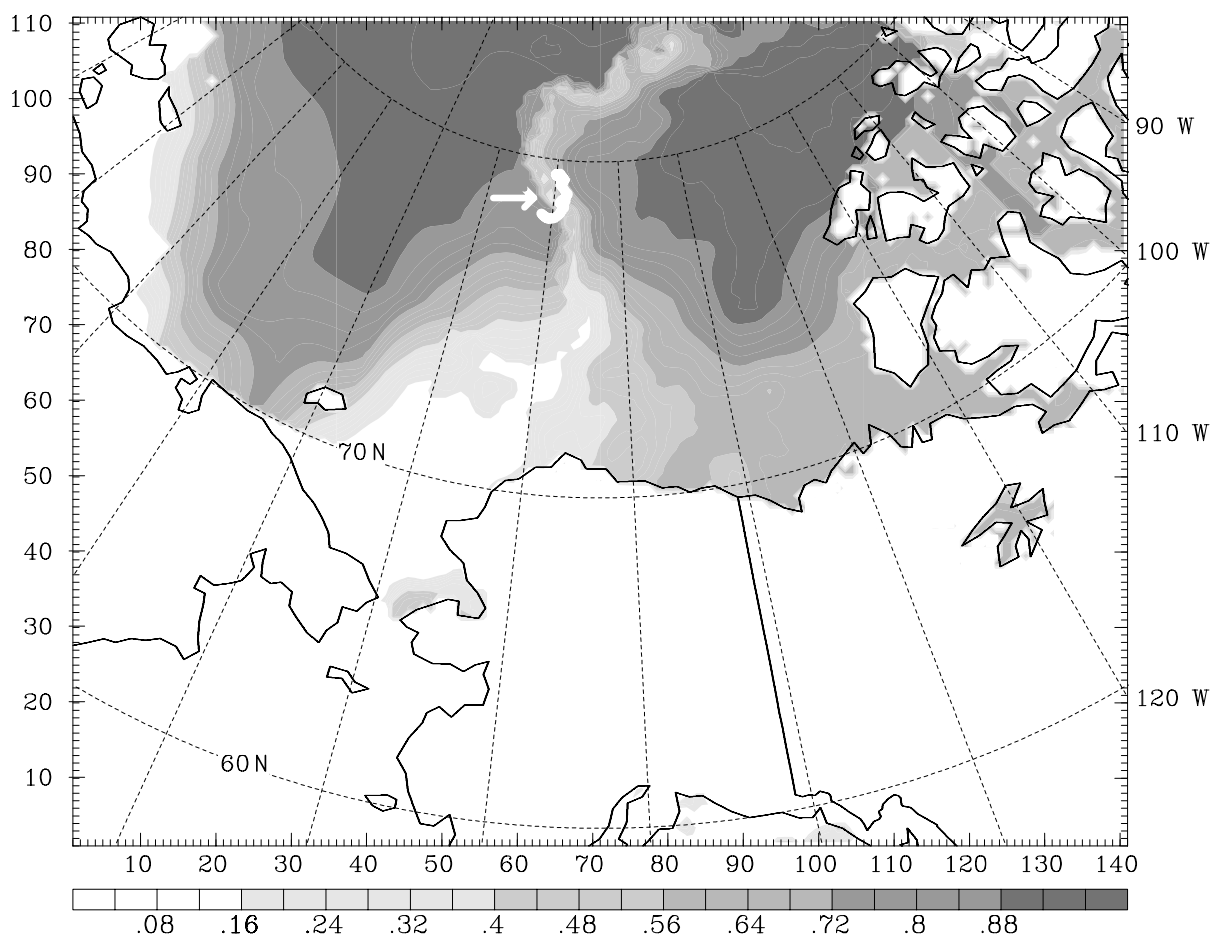
Figure 4. Gray scale of sea-ice fraction during August 1998. The track of Ice Station SHEBA during August is shown next to the arrow in the Arctic pack ice.

output are combined into month-long fields at 3-h intervals. HB found that the 3-h interval well captures the diurnal cycle of incident radiation at Summit, Greenland.

[20] Sea-ice albedo is set at 0.8 for January 1998 when little sunlight reaches the Arctic Ocean grid points. For June 1998, short-wave radiation is crucial for the surface energy balance, so a careful procedure is required. A full treatment of the sea ice surface conditions requires inclusion of a coupled model system. For atmospheric model simulations presented here, however, we have included a specified treatment. A detailed description of the procedure is given in Appendix A, while a brief summary is provided here. The sea-ice albedo during June is taken to be a function of time and latitude. For simplicity, the sea-ice albedo is independent of longitude and the diurnal cycle. The albedo decreases linearly with time from the presnowmelt value 0.82 to the "early July" value 0.50 over a period of 35 days. Onset of the snowmelt on sea ice is determined for each latitude from NSIDC SSM/I brightness temperatures.

[21] For August 1998, the sea-ice fraction of the grid points is considered to represent the bare ice component only, with melt ponds treated as open water. On the basis of observations at SHEBA, the bare ice albedo is set at 0.65 prior to 13 August [*Perovich et al.*, 2002a]. The albedo linearly increases in time from 0.65 to 0.82 for 13 August to 1 September, as freezeup and snow accumulation begin.

4. Results

4.1. Surface Layer Variables at SHEBA

[22] To begin the evaluation of the Polar WRF simulations, we look at the time series of surface pressure for January, June and August 1998 (Figure 5). Furthermore, model performance statistics for several near-surface fields are displayed in Table 1. The closeness between the observed and simulated time series shown in Figure 5 provides an indication that the simulations capture the synoptic variability of the surface pressure with high correlations: 0.99, 0.98, and 0.99 for January, June and August, respectively, and low root mean square errors (RMSE): 2.3, 2.0, and 1.3 hPa, respectively. Also, the biases are small, between 0.4 and 1.2 hPa. It is probable that the assimilation of the SHEBA observations into ERA-40 has contributed to the quality of the initial conditions for the simulations, and therefore contributed to the good results seen here. The positive biases are highly influenced by errors in the representation of migrating low-pressure systems, including those on 4−5 January and 20 June.
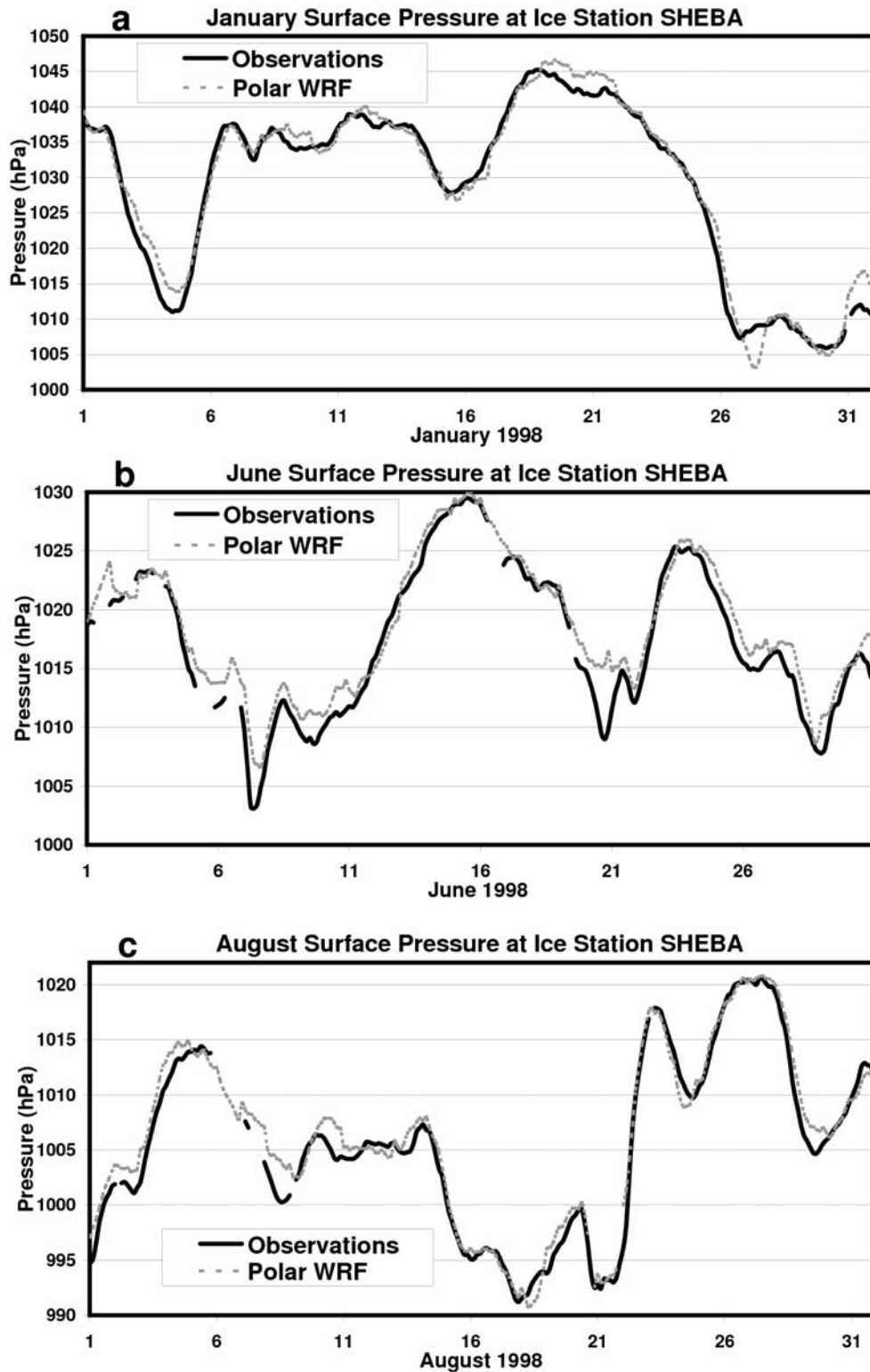
Figure 5. Surface pressure (hPa) from observations and Polar WRF at Ice Station SHEBA for (a) January 1998, (b) June 1998, and (c) August 1998.

[23] While the pressure field is strongly influenced by the synoptic variations, the lower boundary layer temperature is much more heavily influenced by local diabatic processes associated with the surface energy balance. Figure 6 shows time series for temperature at the surface and 2.5 m (observed)/2.0 m (simulated) above sea level (ASL). Given the complexities in simulating the near-surface temperature, Polar WRF produces very reasonable results in Figure 6.

Table 1. Performance Statistics of Polar WRF for January, June, and August 1998 Compared to Ice Station SHEBA Observations[a]

Variable	Correlation			Bias (Observed Mean)			Root Mean Square Error		
	January	June	August	January	June	August	January	June	August
Surface pressure (hPa)	0.99	0.98	0.99	0.4 (1029.0)	1.2 (1017.3)	0.7 (1005.5)	2.3	2.0	1.3
Surface temperature (°C)	0.82	0.45	047	−1.6 (−30.8)	0.4 (−0.6)	0.1 (−1.1)	4.3	1.1	1.0
2.0/2.5 m temperature[b] (°C)	0.81	0.48	0.61	−1.8 (−29.7)	0.2 (−0.8)	0.1 (−1.3)	4.0	1.1	0.9
10 m temperature[c] (°C)	0.80	0.54	0.64	−2.0 (−29.3)	0.2 (−0.8)	0.0 (−1.2)	4.2	1.1	0.9
Temperature difference between 10 m and surface (K)	0.59	0.19	0.26	0.4 (1.5)	−0.1 (−0.2)	0.0 (−0.2)	1.4	0.7	0.6
10−m wind speed[c] (m s^{-1})	0.89	0.75	0.81	−0.6 (5.2)	−0.6 (4.8)	−0.6 (5.0)	1.5	1.5	1.6
2.0/2.5 m specific humidity (10^{-3})	0.81[b]	0.66[c]	0.67[c]	−0.04[b] (0.29)	0.14[b] (3.38)	0.0[c] (3.41)	0.12[b]	0.29[b]	0.25[c]
Incident longwave radiation (W m^{-2})	0.83	0.48	0.32	−9.1 (169.9)	17.9 (282.3)	3.1 (298.9)	24.3	34.7	23.8
Incident shortwave radiation (W m^{-2})	-	0.81	0.71	-	−9.0 (280.7)	1.1 (115.9)	-	170.9	78.4
Sensible heat flux[c] (W m^{-2})	0.44	0.36	0.20	−9.2 (−6.7)	3.8 (2.4)	4.9 (1.2)	18.1	15.0	9.3
Latent heat flux[c] (W m^{-2})	0.36	0.57	0.29	0.19 (−0.24)	−2.8 (7.0)	−0.1 (1.8)	0.8	6.3	4.3
Friction velocity[c] (m s^{-1})	0.89	0.61	0.80	0.09 (0.19)	0.10 (0.19)	0.05 (0.20)	0.12	0.12	0.08

[a]Monthly mean observed values are shown in parentheses after the bias for the simulations.
[b]Observations interpolated to 2.5 m from tower observations are used to evaluate 2.0-m Polar WRF results.
[c]Observations interpolated to 10 m from tower observations are used to evaluate Polar WRF results.

There is a cold bias of 1.6–2.0 K during January, with a large contribution from errors in the simulation of relatively warm synoptic events between 2 January and 13 January. In comparison to other modeling studies of the SHEBA case, *Inoue et al.* [2006] found similar cold biases of 1.8–2.3 K at the surface during a study of ARCMIP model runs for May 1998. Direct comparison with the various ARCMIP model runs studied by Inoue et al. is not possible as they studied a different month than those simulated with Polar WRF, and the ARCMIP model specifications are also different than those for Polar WRF. During June, the Polar WRF temperature variations in Figures 6c and 6d are small, usually
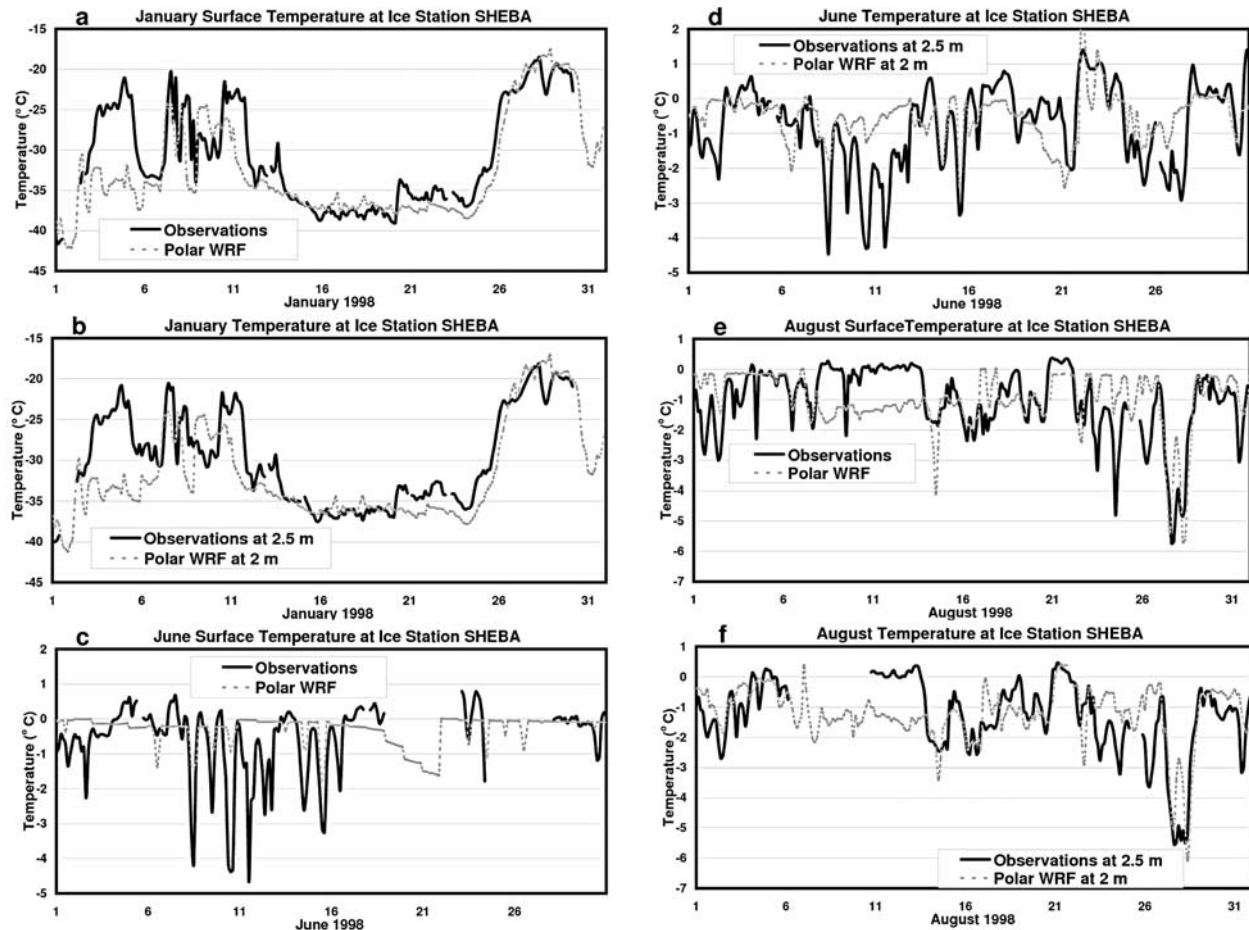

Figure 6. Temperature (°C) from observations and Polar WRF simulation at Ice Station SHEBA for (a and b) January, (c and d) June, and (e and f) August 1998.

within a few degrees of the freezing point. The simulations show a small warm bias of 0.2–0.4 K. Correlations are below 0.55 primarily owing to errors in the representation of high-frequency temperature fluctuations. In particular, several abrupt cold events between 8 and 16 June are not represented, or inadequately represented in the simulation (Figures 6c and 6d). The observed cold events are strongly influenced by radiation and typically peak when the diurnal cycle of incident solar radiation is near a minimum.

[24] During August, the observed temperature at the surface and 10-m ASL primarily stays between −6°C and 0°C. Interpolations of observed quantities to 2.5 m for this month are complicated owing to the consequences of ice melt on tower observation heights. A comparison of simulated temperature to observed temperature reveals very small magnitude biases not exceeding 0.1 K at the surface and 10 m ASL. The RMSE were 1.0 K and 0.9 K, respectively at those levels. Overall, Polar WRF has very well represented the climatology of August 1998 when the near-surface temperature fluctuations are small. Observed and simulated temperatures trend slightly colder in the latter half of August than during the first half, consistent with the transition toward fall conditions.

[25] Wind speeds at 10 m ASL are shown in Figure 7. The synoptic variability is reasonably well captured during the three months, so the correlations are 0.89, 0.75, and 0.81 for January, June and August, respectively. Failure of the simulation to capture the observed speed maximum of 12.1 m s^{-1} on 7 June contributes to the lower correlation for that month. A consistent low wind speed bias of 0.6 m s^{-1} is present. In contrast, the ARCMIP model biases for May 1998 reported by *Inoue et al.* [2006] were positive with larger magnitudes ranging from 1.4 to 3.0 m s^{-1}. Polar WRF's surface roughness length for sea ice, 10^{-3} m, may contribute to its negative speed bias, as this value is larger than most estimates based upon SHEBA observations. *Persson et al.* [2002] provided estimates of surface roughness at SHEBA varying from 3.1 × 10^{-4} to 6.0 × 10^{-4} m on the basis of monthly medians, and 5.7 × 10^{-4} to 10.8 × 10^{-4} m on the basis of monthly means. The ability of Polar WRF to capture the synoptic variability of the lower boundary layer velocity is also demonstrated by Figure 8 which shows the observed and simulated wind direction at 10 m ASL. In summary, Polar WRF is able to provide a good overall simulation of basic meteorological fields for the surface layer during January, the early summer month June and the late summer month August of the SHEBA study.

4.2. Impact of Fractional Sea Ice

[26] To test the impact of the inclusion of fractional sea ice on the Polar WRF simulations, we consider January 1998 when the difference in surface temperature between open water and ice is much greater than during the summer months. During this winter month, the surface temperature of open water is typically about −1.8°C, while that of ice is frequently less than −30°C and temporarily reached −40°C during SHEBA. Consequently, a small open-water fraction can have dramatic effect on surface-layer fluxes during the Polar Night [*Lüpkes et al.*, 2008]. On the other hand, the impact on the simulations is mitigated near SHEBA by the especially small fraction of open water present locally during January. *Overland et al.* [2000], however, noted that

the observed surface temperature and sensible heat flux near SHEBA varied depending on the local thickness of sea ice. Thickness variation is not considered in the present study.

[27] A comparison of the results for the January 1998 simulation without open water fraction to the January simulation shown previously in Figures 5–8 is presented in Table 2. Simulated values are evaluated in comparison to the observations at Ice Station SHEBA. The simulation without fractional sea ice has prescribed 100% ice cover for oceanic grid points with 50% or more sea-ice cover from the same input field used in the other January simulation. If the sea-ice fraction from the input field was less than 50%, the new simulation specifies the grid point to be 100% open water. This specification for the new simulation results in 100% ice cover for all the grid points close to the track of SHEBA during January. Table 2 shows that the simulated impact of the inclusion of open water fraction is very small at Ice Station SHEBA for January.

[28] To demonstrate that the specification of open water fraction can be significant we have also included values for the grid point at 72.28°N, 167.65°W in the right column of Table 2. The location of this point is shown by the cross inside a square displayed in Figure 1. The point had one of the highest open water fractions during January for locations in the Arctic Ocean within several hundred kilometers of Ice Station SHEBA. Overall, the average sea-ice fraction at the point was 89% for January, but was reduced to 62% for the selected study period from 0000 UTC 18 January to 0000 UTC 25 January. The surface temperature at the grid point was 4.1 K warmer in the January simulation with fractional sea ice than in the simulation without fractional sea ice for the monthly average. The difference, however, increased to 14.3 K for the study period. Note that the sign of sensible heat flux differs at the point between the two January simulations (Table 2). In particular, the heat flux is 146.0 W m^{-2} from the warmer surface to atmosphere during the study period in the simulation with fractional sea ice, but is 40.0 W m^{-2} from the atmosphere to the colder surface without fractional sea ice.

4.3. Surface Energy Balance

[29] Table 1 includes model performance statistics for several surface energy balance fields. Estimates of sensible heat flux, latent heat flux and friction velocity from the tower observations interpolated to 10 m are used for our evaluations in Table 1. During January, the main energy balance at the surface in WRF is between the net long-wave radiative cooling, 28.3 W m^{-2}, turbulent heat flux downward from the atmosphere, 14.6 W m^{-2}, and heat flux upward through the ice 13.6 W m^{-2}. In contrast, the observational estimates in the SHEBA surface flux file show an average downward turbulent heat flux of 6.7 W m^{-2} on the basis of the tower observations interpolated to 10 m ASL. The greater magnitude for the simulated heat flux is consistent with the bias inferred from Figure 9 (discussed below). Moreover, the friction velocity (u$_*$) for the simulation, 0.28 m s^{-1}, exceeds the observed estimate by 0.09 m s^{-1}. The latter error is not only present during the stably stratified January conditions. A similar error is found for June, when the vertical temperature gradient is reversed within the surface boundary layer (Table 1). The magni-
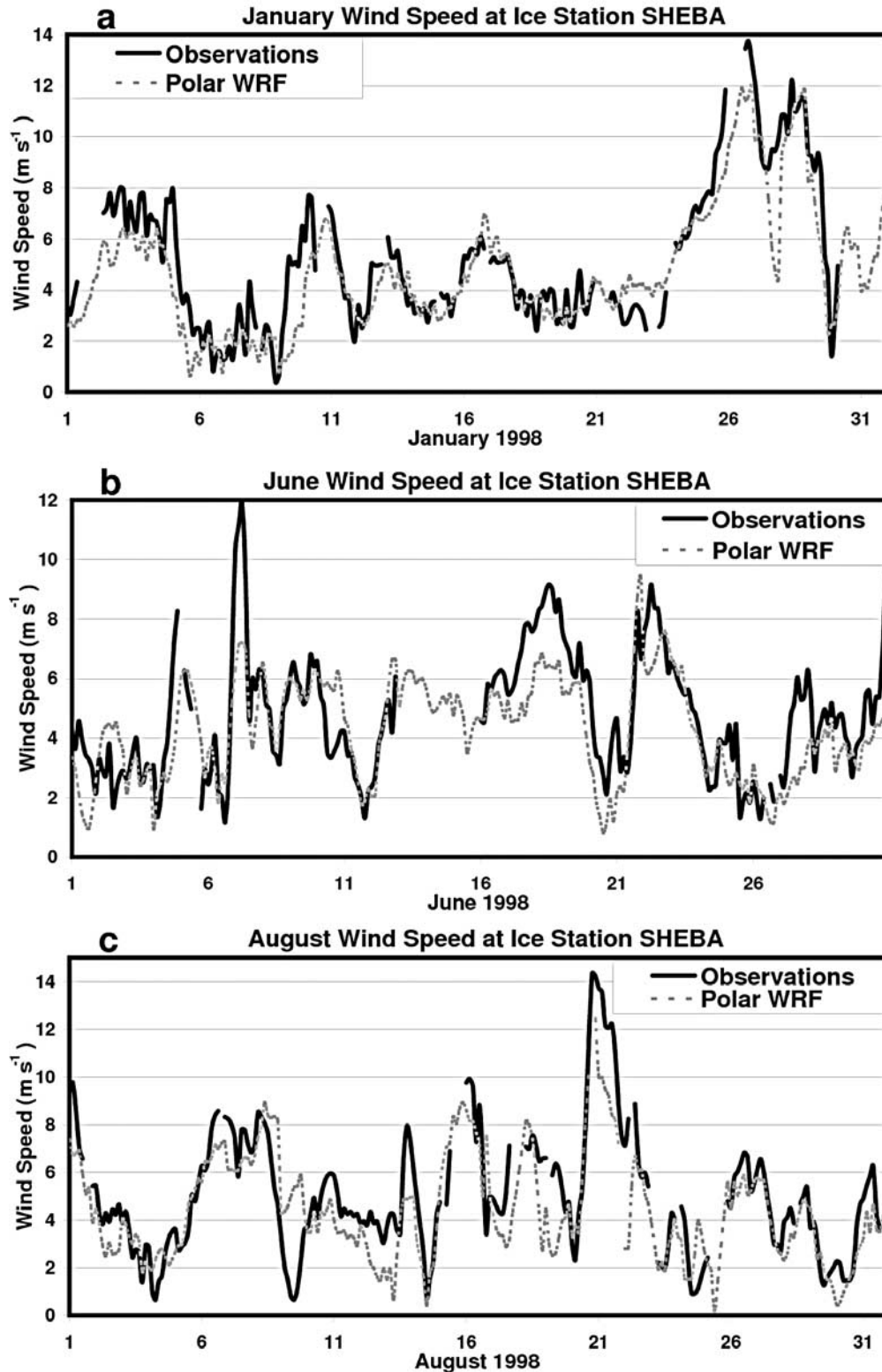
Figure 7. Ten-meter wind speed (m s^{-1}) from observations and the Polar WRF simulation at Ice Station SHEBA for (a) January, (b) June, and (c) August 1998.

tude of the average simulated latent heat flux is less than 0.1 W m^{-2} for the winter month. Furthermore, Polar WRF's January incident long-wave radiation at the surface is 9.1 W m^{-2} less than that of the observations. Thus, the lower-than-observed incident long-wave radiation is at least partially compensated by an erroneously large downward sensible heat flux. About one third of the overall monthly bias for incident long-wave radiation is contributed by the
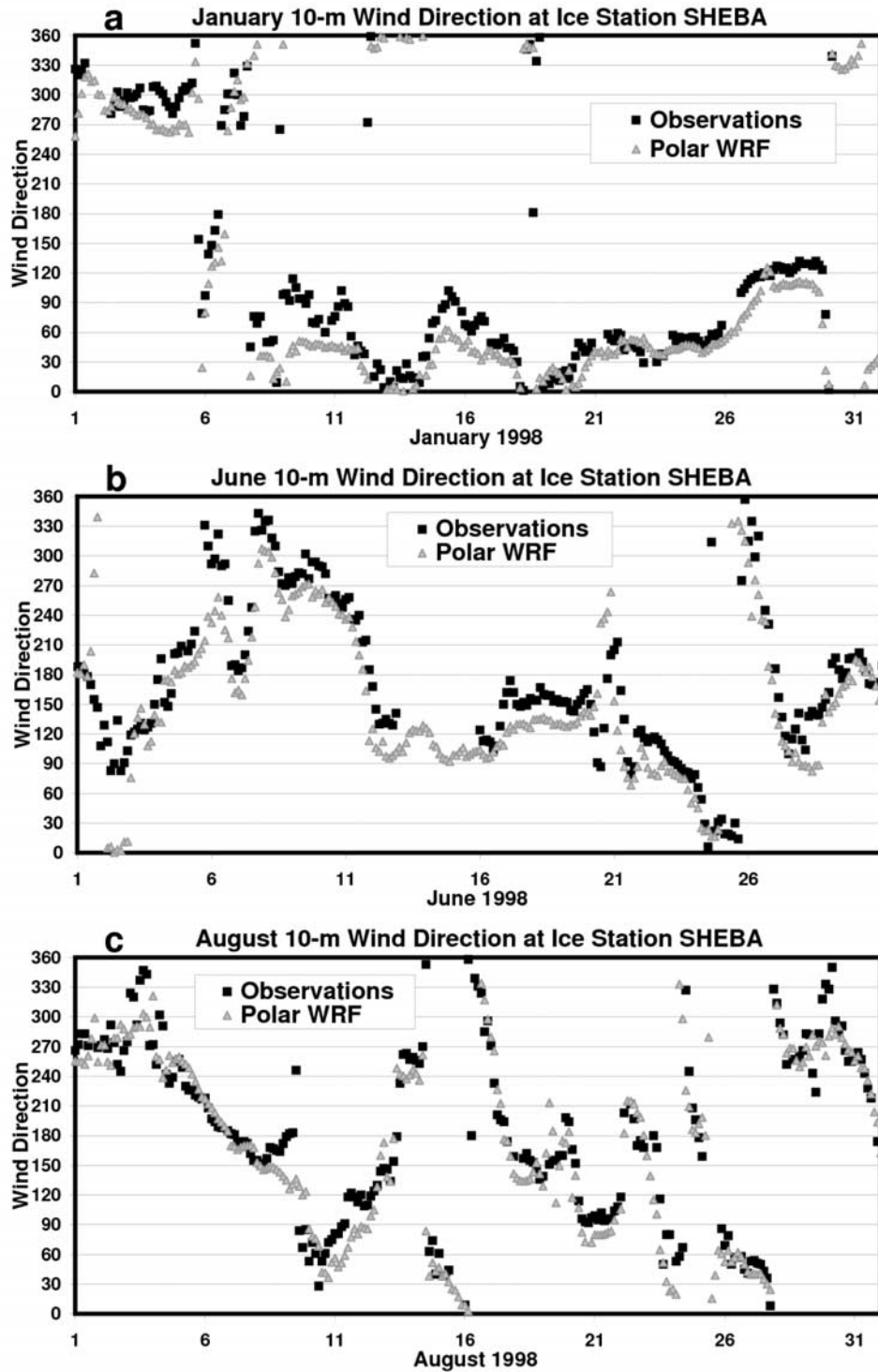
Figure 8. Ten-meter wind direction (degrees from true north) from observations and the Polar WRF simulation at Ice Station SHEBA for (a) January, (b) June, and (c) August 1998.

period between 1200 UTC 3 January and 0000 UTC 7 January, when the model did not simulate the observed liquid water cloud characteristics. About another third of the incident long-wave bias is contributed by time period between 1200 UTC 10 January and 0000 UTC 14 January. Together, these two periods contribute toward 73% of the overall cold bias at the surface during the winter month.

[30] Figure 9 shows a scatterplot of the sensible heat flux divided by the 10-m wind speed against the difference between the surface temperature and the 10-m temperature. The temperature difference is plotted as positive for an unstably stratified surface layer. Figure 9 is analogous to Figure 13 of *Tjernström et al.* [2005]. They note that with the bulk aerodynamic method, the sensible heat flux should

Table 2. Comparison of Polar WRF Simulations for January 1998 With and Without Fractional Sea Ice[a]

Variable	Mean Observed Value at SHEBA	Correlation		Bias		RMSE		Mean WRF Value at 72.28°N, 167.65°W	
Surface pressure (hPa)	1030.1	0.98	0.98	0.5	0.9	2.2	2.3	1027.9	1027.4
								1034.3	1033.4
Surface temperature (°C)	−31.0	0.83	0.81	−2.2	−2.3	4.3	4.3	−27.5	−31.6
								−17.3	−31.6
2.0/2.5 m specific humidity (10^{-3})	0.26	0.82	0.77	−0.04	−0.04	0.12	0.11	0.30	0.25
								0.42	0.23
10-m wind speed (m s^{-1})	5.3	0.88	0.90	−0.6	−0.5	1.5	1.3	6.2	5.8
								10.5	8.4
Sensible heat flux (W m^{-2})	−0.7	0.08	0.20	−13.9	−14.3	18.1	18.1	29.8	−19.1
								146.0	−40.0

[a]Simulated values for Ice Station SHEBA are evaluated by comparisons to the observations. The first (second) values shown for bias, correlation, RMSE, and the grid point 72.28°N, 167.65°W are for the simulation with (without) fractional sea ice. For 72.28°N, 167.65°W, the top row values are the monthly average. The bottom row values are the average for 0000 UTC 18 January to 0000 UTC 25 January.

be proportional to both the surface layer wind speed and the temperature difference. The squares show the observed values for the normalized heat flux. It is apparent from Figure 9 that the magnitude of the heat transfer coefficient for Polar WRF with the MYJ boundary layer parameterization, shown by the triangles, is excessive for both stable and unstable profiles. For stably stratified conditions, the observed normalized heat flux shows little dependence on the surface layer temperature difference. *Grachev et al.* [2005] investigated the stable surface boundary layer at SHEBA and found several different regimes, with unconventional turbulent structures for the most stable cases. More than one stable regime is apparent in Figure 9. The difference between observed stable and unstable conditions was discussed by *Tjernström et al.* [2005]. Polar WRF shows smaller magnitude normalized heat fluxes in stable regime compared to the unstable regime for the similar magnitude temperature difference, but does not capture the relative independence from the temperature difference seen in the highly stably stratified observed cases.

[31] Figure 10 shows vertical profiles of the monthly average temperature at SHEBA for January and June. Observed rawinsonde soundings are provided by the NCAR Earth Observing Laboratory under sponsorship of the National Science Foundation. Soundings were available twice per day for most days during the 3 months studied here. The first four days of June had four soundings per day. During January, the model's initial conditions, shown as the Hour 00 curve in Figure 10a, well match the observed temperature profile. Initial conditions are taken from ERA-40 reanalyses, which are influenced by observed soundings at SHEBA. Considerable boundary layer adjustment, however,
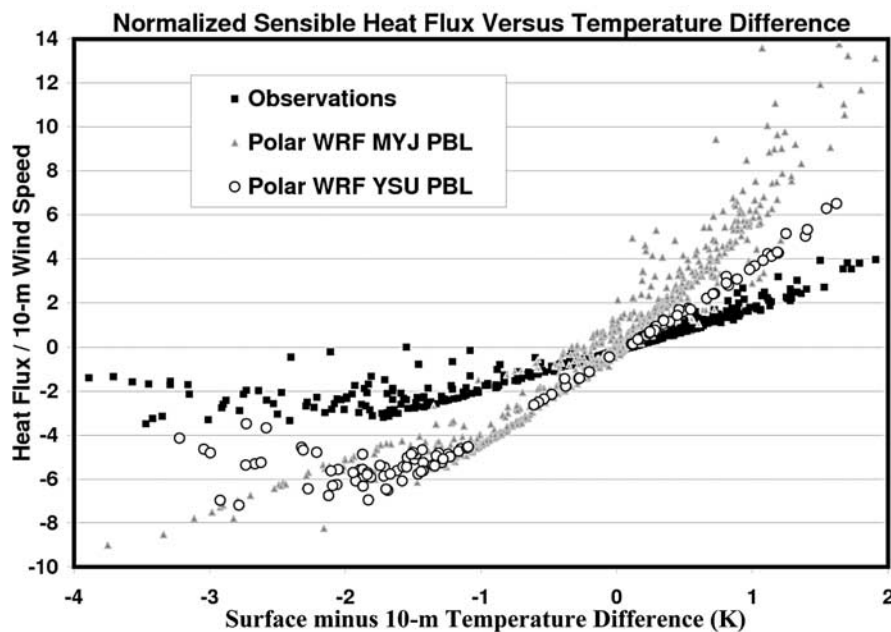

Figure 9. Scatterplot of sensible heat flux divided by 10-m wind speed (kg m^{-1} s^{-2}, vertical axis) and the temperature difference between the surface and 10 m (K, horizontal axis) for the observations and the Polar WRF simulations with the Mellor-Yamada-Janjic (MYJ) and Yonsei University (YSU) boundary layer parameterizations.
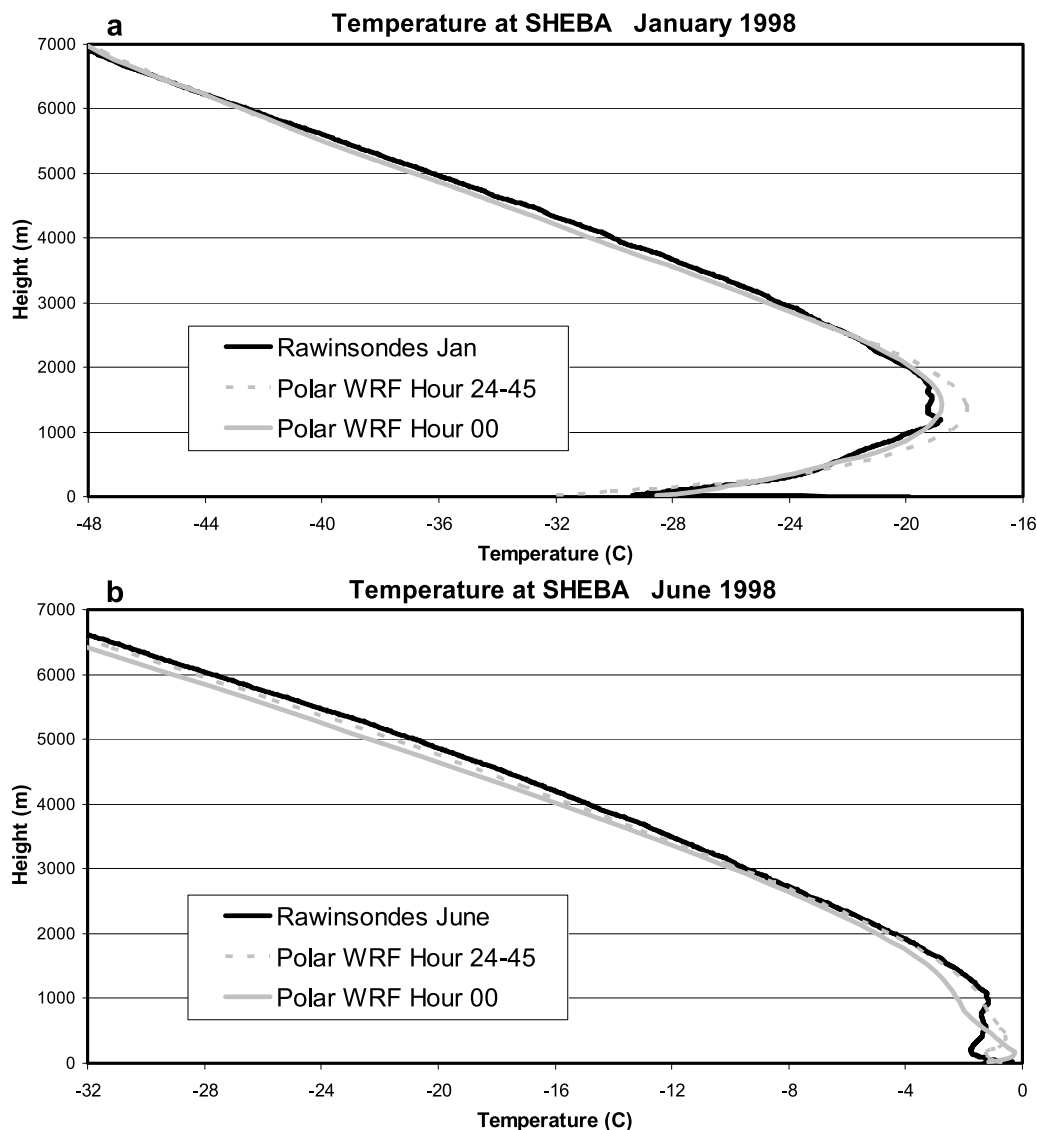
Figure 10. Vertical profiles of monthly average temperature (°C) from observations and the Polar WRF simulations at Ice Station SHEBA for (a) January and (b) June 1998. The black line shows temperature from rawinsonde observations. The solid gray line shows Polar WRF initial conditions, and the dashed gray line shows the results after spin-up.

often occurs within the first 24 h of a polar simulation [e.g., *Parish*, 1984]. During the reported part of the simulations, shown as the Hour 24–45 curve and after at least 24 h of spin-up, the temperature at the top of the lower tropospheric inversion has spuriously warmed by approximately a degree to −17.9°C at 1416 m ASL. Below 300 m ASL, simulated temperature cools during spin-up, resulting in the surface cold bias seen in Table 1. At higher levels, little drift in temperature during the simulation is seen in Figure 10a.

[32] In Figure 10b, the simulated temperature profile for June after spin-up is actually much closer to the observed profile than the model initial conditions. The correction is especially apparent between 1000 and 2500 m. The initial conditions are colder than the observed profile by about 1 K in the middle troposphere. The model atmosphere warms during spin-up and corrects for most of this difference. Furthermore, the initial relative humidity profile (not shown)

indicates that the middle troposphere is initialized with excess water vapor for June simulations. The results for August are not shown in Figure 10, however, the profiles for this month are strikingly similar to those for June. Analogous to the results for the temperature profile shown in Figure 10b, the relative humidity error during June is reduced during model spin-up. The errors in the atmospheric moisture field, however, could impact the atmospheric radiative transfer discussed in the following paragraphs.

[33] Figure 11 demonstrates that the error in the simulation of incident long-wave radiation is episodic, suggesting the influence of clouds. In particular, the greatest simulation minus observation magnitude that persists over a period of at least 24 h occurs after 1200 UTC on 3 January and lasts until late 4 January. During this time the simulated near-surface temperatures are much colder than those observed. Specifically, the average observed surface temperature
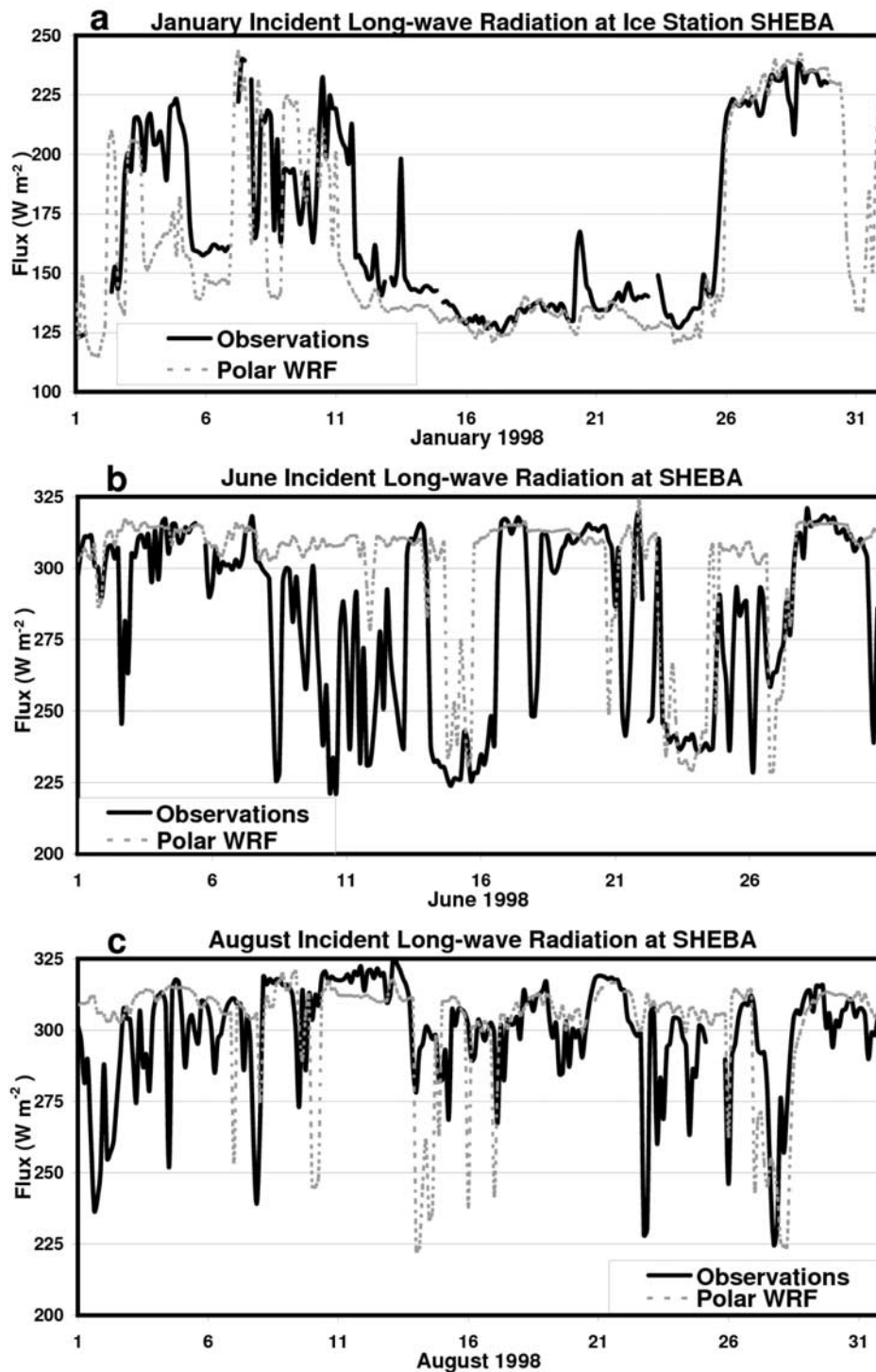
Figure 11. Incident long-wave radiation (W m^{-2}) from observations and the Polar WRF simulation at Ice Station SHEBA for (a) January, (b) June, and (c) August 1998.

between 1500 UTC 3 January and 2100 UTC 4 January is −23.5°C. For the simulation, the surface temperature is −34.4°C. Consideration of the long-wave radiation appears to be critical for understanding how such temperature contrasts occur. For example, the observed warmer days during January correspond to days of increased incident long-wave radiation in Figure 11 (e.g., P. O. G. Persson et al., Observations of large thermal transitions during the Arctic night from a suite of sensors at SHEBA, paper presented at 5th Conference on Polar Meteorology and Oceanography, American Meteorological Society, Dallas, Texas, 1999a). The observed incident long-wave radiation during the 1500 UTC 3 January to 2100 UTC 4 January time period averages 209.4 W m^{-2}, much greater than the
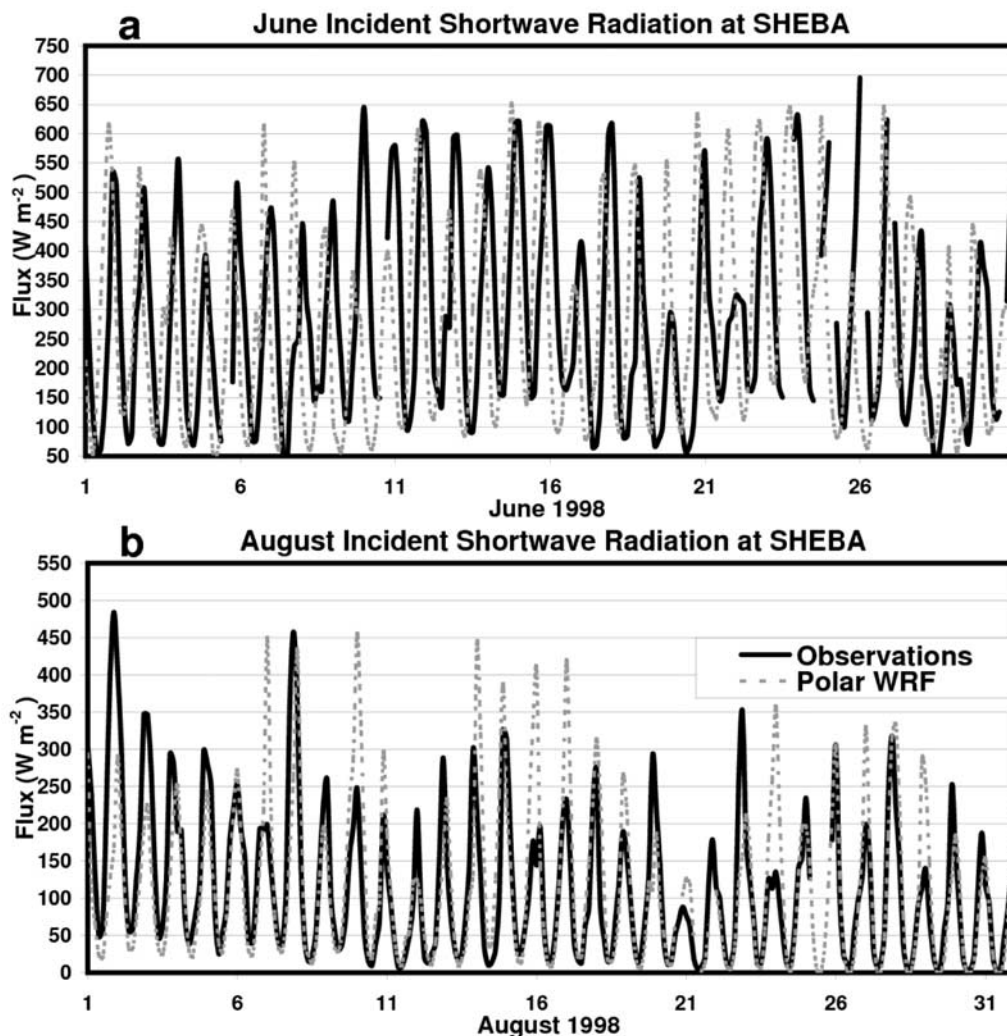
Figure 12. Incident short-wave radiation (W m^{-2}) from observations and the Polar WRF simulation at Ice Station SHEBA for (a) June and (b) August 1998.

simulated 161.5 W m^{-2}. The apparent reason for the difference is discussed below.

[34] During June 1998, near-surface temperature is highly influenced by the diurnal cycle of incident short-wave radiation (Figures 6 and 12). There is a small positive bias in the overall monthly average temperature in the near-surface atmospheric layer (Table 1). The average bias for incident short-wave (long-wave) radiation at the surface is −9.0 (17.9) W m^{-2}. The average sensible heat flux (positive from the surface to the atmosphere) is small in the observations, 2.4 W m^{-2}. Polar WRF shows a positive bias of 3.8 W m^{-2} for sensible heat flux. Corresponding to the increased sensible heat flux in the simulation is an approximately 50% greater difference in surface layer temperature between the Earth's surface and the typically colder atmosphere at 10 m ASL, compared to the observed values.

[35] The difference between the simulation and the observations is especially enhanced for several very brief cold events shown in Figure 6 during 7−17 June, with WRF not being able to reproduce adequate cooling. Excessive simulated cloud cover appears to be the reason for the difference.

Figure 13 shows the observations of temperature and cloud fraction from Canadian Coast Guard ice breaker Des Groseilliers within the pack ice near Ice Station SHEBA. The horizontal axis is time with the tic marks at 0000 UTC. Local midnight lags 0000 UTC by about 11 h at SHEBA during June. The surface ship report data were provided by the SHEBA Project Office at the University of Washington. As demonstrated in Figure 13, the observed cold events tend to be times of reduced cloud fraction. Furthermore, observed incident long-wave radiation is reduced during the cold events that are not reproduced by WRF (Figure 11). Additionally, observed incident short-wave radiation tends to be greater than the corresponding Polar WRF values shown in Figure 12 during these time periods. As WRF's cloud treatment does not assign fractional coverage when clouds are present, an alternative approach is taken to demonstrate that clouds contribute to the differences between the simulation and observations at SHEBA during 7−17 June.

[36] Vertically integrated retrievals of liquid water path (LWP) and ice water path (IWP) for SHEBA have been
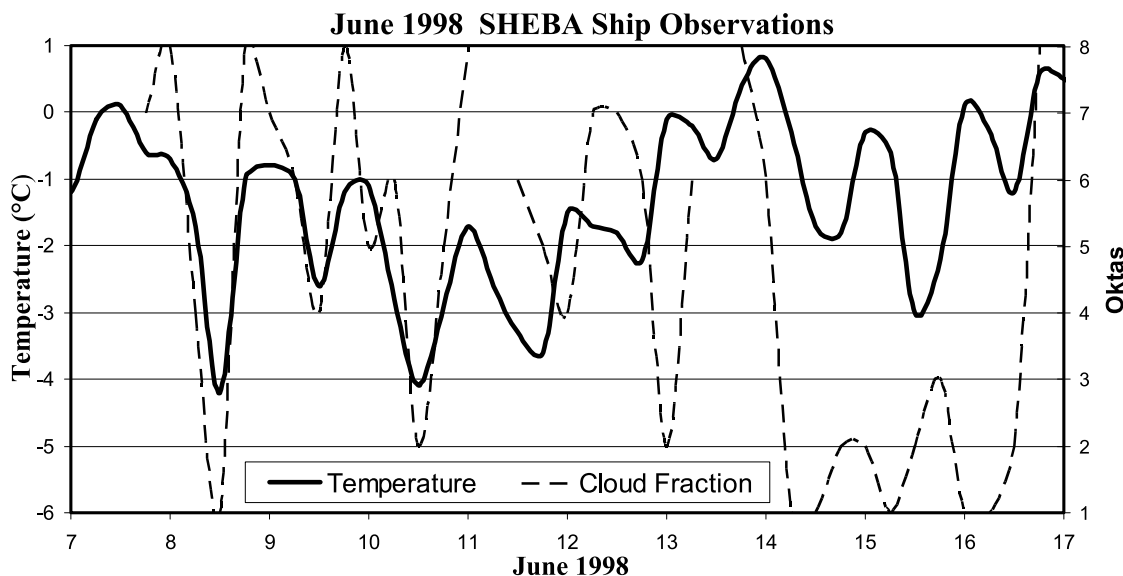
June 1998 SHEBA Ship Observations

Figure 13.   Ship observations at Ice Station SHEBA of temperature (°C) and cloud fraction (oktas) for 7−17 June 1998.

supplied by Matthew Shupe [*Shupe et al.*, 2005]. The LWP is derived from two-channel microwave radiometer observations of sky brightness temperature. The uncertainty in the LWP retrievals is about 0.025 kg m^{-2}. Thus, the retrievals must be used with caution during wintertime when the uncertainty is often greater than actual values for wintertime liquid clouds (M. Shupe, personal communication, 2007). The IWP is derived from 35 GHz radar reflectivity, and its uncertainty is similar to observed magnitudes of this field. Figure 14 shows vertically integrated values of LWP and IWP for the observations and water

paths for snow, ice cloud and liquid water cloud from the Polar WRF simulation. Simulated water paths for rain and graupel are very small and not shown. The results in Figure 14 show persistent liquid water clouds with LWP values 0.1−0.3 kg m^{-2} are present in the simulation for 8−11 June. The observations, however, do not show persistent water or ice clouds during this time. The excessive long-wave radiation from the persistent simulated water cloud explains the failure to capture the acute cold events during this period.

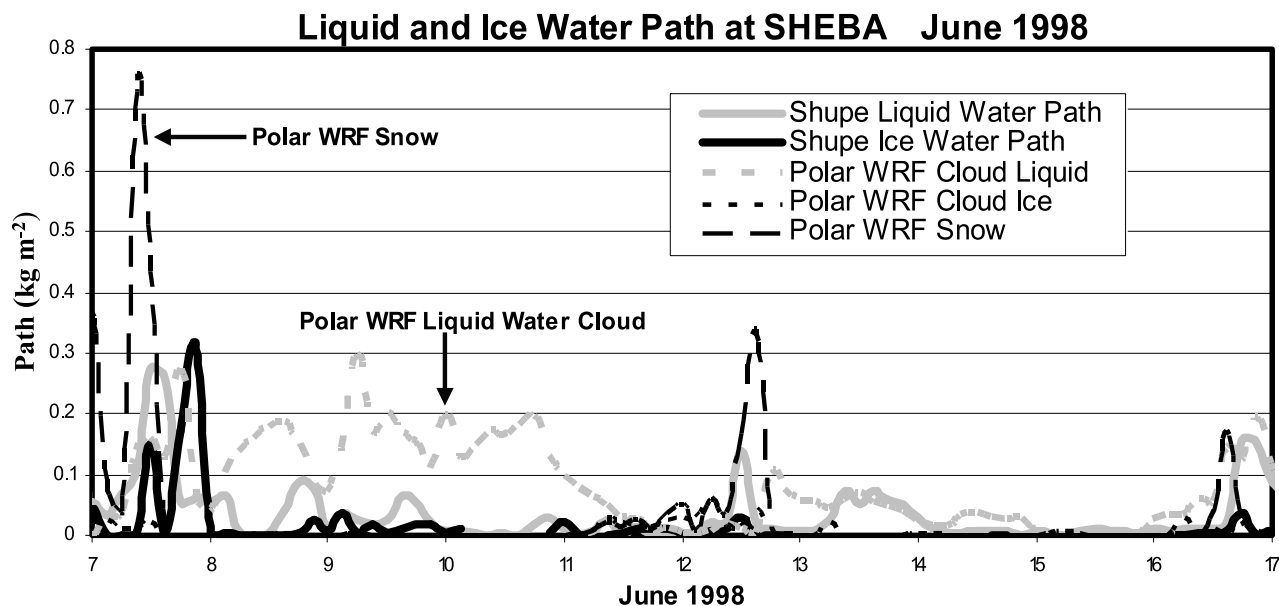## Liquid and Ice Water Path at SHEBA   June 1998

Figure 14.   Liquid water path (kg m^{-2}) and ice water paths at Ice Station SHEBA from vertically integrated cloud observations of *Shupe et al.* [2005] and Polar WRF simulation of liquid cloud, ice cloud, and snow for 7−17 June 1998.

[37] A similar comparison (not shown) for January 1998 suggests that an alternative case occurs during the winter month. A migrating low-pressure system passes to the north of Ice Station SHEBA around 4 January. The passage is simulated by Polar WRF, though the intensity of the surface pressure minima at SHEBA is underrepresented by a few hPa in Figure 5a. Associated with the migrating weather system, liquid water cloud is present for the observed fields during 1500 UTC 03 January to 2100 UTC 04 January. The average measured liquid water path is 0.029 kg m^{-2} during this time. The simulated value is only 0.00019 kg m^{-2}, consistent with the tendency for ARCMIP models to significantly undersimulate liquid cloud during Arctic winter [*Prenni et al.*, 2007]. *Shupe and Intrieri* [2004] demonstrated that even small amounts of wintertime liquid cloud amount have very strong impact on the long-wave radiative balance. Thus, the incident long-wave radiation and surface temperature are much higher in the observations than in the simulation. Some caution must be applied owing to the large uncertainty in observed retrievals. Furthermore, the cold temperature bias persists for a few days and does not immediately disappear even with the rapidly increasing pressure after 4 January. Nevertheless, the results suggest the importance of capturing the cloud physics over the Arctic Ocean. For August 1998, the biases and root mean square errors for the radiation terms and the latent heat flux shown in Table 1 are smaller than the corresponding values for June.

4.4. Sensitivity to Physical Parameterizations

[38] In HB, the physical parameterizations for the LSM, boundary layer, and microphysics parameterizations were extensively tested to find the set of parameterizations best suited for the Greenland Ice Sheet. On the basis of those tests, the MYJ PBL, the Noah LSM, the RRTM long-wave radiation code and the Goddard short-wave radiation code were selected. These parameterizations have been applied to the present study for the Arctic Ocean region, with the addition of the advanced two-moment Morrison microphysics scheme. Limited sensitivity tests are now performed to consider whether the selected set of parameterizations is optimal over the western Arctic domain. Three case studies are used. The first is 18–27 January that includes an extended cold period at Ice Station SHEBA (Figure 6). The second is 8–14 June when high-frequency surface temperature fluctuations linked to the diurnal cycle were observed. Six new simulations are performed for these two case studies, three for each case study period. The sensitivity simulations consider the following changes: (1) The Morrison microphysics replaced by the *Thompson et al.* [2004] scheme that is two-moment for liquid water and one-moment for ice, (2) the Morrison microphysics is replaced by the WRF single-moment five-class scheme (WRFSM) [*Hong et al.*, 2004], and (3) the MYJ boundary layer parameterization is replaced by the Yonsei University (YSU) scheme [*Hong et al.*, 2006]. Model performance statistics compared to the SHEBA observations for the previous (Control) simulations and the new sensitivity simulations are shown in Table 3. Overall, the impact of selection of physical parameterizations is small in sensitivity simulations. The Control configuration tends to have the smallest root mean square errors for state variables during the 18–27 January test. The Control and the simulation with the YSU PBL show similar statistics for the state variables during the 8–14 June test. For the flux terms, the YSU PBL reduces the root mean square errors and bias magnitude for short-wave radiation and sensible heat flux during the latter period. The improvement in short-wave radiation bias is especially large, with values of −65.0 and −25.8 W m^{-2} for the Control and YSU simulations, respectively. Furthermore, simulations with the YSU PBL, shown by the open circles in Figure 9, produce normalized sensible heat fluxes closer to the observed values for the unstable case. Figure 9 also suggests the YSU PBL may produce more realistic heat fluxes for the highly stable case when the surface temperature is more than 2 K colder than the 10-m temperature. Over Greenland, HB found that the MYJ PBL was slightly superior to the YSU scheme. Thus, the preferred boundary layer parameterization appears to depend upon the application.

[39] Otherwise, the sensitivity simulations failed to properly capture the brief cold periods (not shown) during the June test and produced results similar to those seen in Figure 6, thus the warm biases are all similar, 0.8–0.9 K, for this test. The root mean square errors during the test periods are frequently higher during the January sensitivity simulations with the *Thompson et al.* [2004] and WRFSM schemes than for the Control with the more advanced Morrison microphysics, supporting this addition to Polar WRF. The overall small sensitivity to these particular physics parameterizations is consistent with the findings of independent WRF simulations of the Arctic (J. Cassano, personal communication, 2008).

[40] An additional case study is performed for early January 1998 when the simulated near-surface temperature is much colder than the observed value (Figure 6). The sensitivity simulations include replacing the microphysics scheme with (1) the *Thompson et al.* [2004], and (2) the WRFSM schemes as above. A third sensitivity simulation replaces the standard Morrison microphysics (set for aerosol concentrations representative of midlatitude conditions) with a much reduced ice nuclei setting suggested by Hugh Morrison (personal communication, 2008) on the basis of the fall 2004 Mixed Phase Arctic Cloud Experiment (M-PACE) [*Morrison et al.*, 2008]. Only the period from 0000 UTC 3 January to 1200 UTC 5 January is considered for the evaluation. During this period, substantial observed liquid water is present, and the simulation's temperature error in Figure 6 is very large. The results of these sensitivity simulations are not shown here as the results were roughly similar to the control simulation. Overall, the sensitivity to these microphysics schemes appears to be small.

5. Summary and Conclusions

[41] The development of Polar WRF provides an improved model for Arctic climate and synoptic applications. This development, beginning with HB, included evaluations and modifications for polar applications of the boundary layer parameterization, cloud physics, snow surface physics and sea-ice treatment. The simulations of winter and summer conditions over the Greenland Ice Sheet by HB led to adjustments for the Noah land surface model including improved energy balance and heat transfer near

Table 3. Performance Statistics of 18–27 January, and 8–14 June Sensitivity Tests With Different Physics Packages[a]

Variable	18–27 January 2008 Simulations				8–14 June 2008 Simulations			
	Control	Thompson et al. [2004] Microphysics	WRFSM Five-Class Microphysics	YSU PBL	Control	Thompson et al. [2004] Microphysics	WRFSM Five-Class Microphysics	YSU PBL
Surface pressure (hPa)	1.1	1.8	1.9	1.5	1.0	1.1	1.0	1.0
	0.99	0.99	0.99	0.99	0.98	0.97	0.97	0.98
	1.8	2.4	2.5	2.3	1.5	1.7	1.6	1.5
Surface temperature (°C)	−1.3	−2.0	−2.1	−1.3	0.9	0.9	0.8	0.9
	0.93	0.93	0.92	0.95	0.46	0.31	0.49	0.48
	2.1	2.8	2.9	2.2	1.5	1.6	1.5	1.5
2.0/2.5 m temperature (°C)	−1.5	−2.2	−2.3	−1.2	1.1	1.2	1.1	1.0
	0.92	0.91	0.90	0.93	0.26	−0.02	0.25	0.43
	2.3	2.9	3.0	2.1	1.6	1.8	1.7	1.5
10-m wind speed (m s^{-1})	−0.2	−0.5	−0.5	−0.6	0.4	0.3	0.5	0.1
	0.96	0.94	0.93	0.94	0.81	0.82	0.78	0.80
	1.0	1.6	1.6	1.8	1.0	0.9	1.0	0.9
2.0/2.5 m specific humidity (10^{-3})	−0.02	−0.04	−0.05	−0.02	0.32	0.30	0.24	0.27
	0.92	0.91	0.93	0.93	0.15	−0.23	0.06	0.44
	0.05	0.08	0.08	0.06	0.42	0.45	0.39	0.36
Incident long-wave radiation (W m^{-2})	−7.1	−9.5	−10.2	−7.3	37.2	35.0	32.6	29.9
	0.93	0.94	0.90	0.95	0.15	0.13	−0.07	−0.28
	13.0	14.1	16.1	12.0	46.4	44.8	44.9	46.1
Incident short-wave radiation (W m^{-2})	-	-	-	-	−65.0	−40.9	−28.2	−25.8
					0.34	0.29	0.54	0.46
					107.9	82.8	86.4	90.6
Sensible heat flux (W m^{-2})	−13.0	−11.9	−12.5	−13.8	7.9	3.4	6.0	4.1
	0.31	0.53	0.53	0.59	0.34	0.29	0.54	0.46
	15.3	13.3	14.2	15.4	12.4	9.5	9.9	9.4
Latent heat flux (W m^{-2})	0.19	0.02	0.49	0.14	−0.95	2.14	4.99	−2.23
	0.53	0.52	0.36	0.42	0.70	0.65	0.50	0.75
	0.50	0.32	0.57	0.37	5.6	6.3	9.2	6.7

[a]Control has the *Morrison et al.* [2005] microphysics and the MYJ planetary boundary layer. Bias and correlation are calculated compared to SHEBA observations, similar to Table 1. The first value is bias, the second value is correlation, and the third value is root mean square error.

the surface of the persistent snowpack. The present paper continues the work with a series of Arctic simulations to emphasize the role of sea ice for model performance in the polar regions.

[42] In the simulations presented here, Polar WRF is based upon WRF version 2.2. The 141 × 111 horizontal domain over the western Arctic has 25-km horizontal resolution and includes Alaska and parts of eastern Siberia and northwestern Canada. The domain, similar to that used for the ARCMIP study, also includes a large area of the Arctic Ocean that surrounds the October 1997 to October 1998 track of Ice Station SHEBA. Ocean surface treatment is modified to include fractional sea ice, analogous to a previous improvement for Polar MM5. The Polar WRF simulations consist of a series of 48-h integrations initialized daily at 0000 UTC. Initial conditions are taken from the reanalysis fields of ERA-40. Since the SHEBA observations are assimilated by ERA-40, the initial conditions should be high quality near that site. The initial day is taken as model spin-up time for the atmospheric hydrology and boundary layer processes. Model output beginning with hour 24 of the individual simulations is connected into a month-long representation at 3-h intervals. Arctic conditions are simulated for the selected months: January 1998, June 1998, and August 1998 representing midwinter, early summer and late summer conditions, respectively.

[43] Owing to the high sensitivity of the summer surface energy balance to the reflectivity of solar radiation by the sea-ice surface, care is taken to specify the temporal and latitudinal variability of sea-ice albedo (see Appendix A). For simplicity, longitudinal variations in sea-ice albedo are

not considered. During January 1998, when much of the Arctic Ocean is encompassed by the Polar Night, snow and ice albedo values are simply set at 0.80. Inspired by remote-sensing and SHEBA observations, the albedo of sea ice (including developing melt ponds) is specified as a function of time and latitude for June, decreasing from premelt value of 0.82, and decreasing linearly over 35 days toward 0.5, representing early July conditions. Estimates of the onset of snowmelt on sea ice, as a function of latitude, are provided by NSIDC fields derived from SSM/I brightness temperatures. During August 1998, when melt ponds tend to be deeper and likely to be detected as open water by remote sensing observations, the albedo over Arctic sea ice is prescribed on the basis of averaged tower observations at Ice Station SHEBA. During this month, the albedo of bare ice (excluding melt ponds) is taken as a constant 0.65 until 12 August. Beginning on 13 August, the prescribed albedo increases linearly with time from 0.65 to 0.82 on 1 September, as freezeup proceeds during the transition toward fall conditions.

[44] Results for the January, June and August simulations are compared with the observations of the drifting SHEBA station within the Arctic sea ice. The Polar WRF simulations show good agreement with observations for all three months. Some differences between the simulations and observation occur owing to apparent errors in the synoptic forecasts and the representation of clouds. Nevertheless, the biases for the majority of simulated fields are very small. The results, however, also demonstrate that simulating the ice and water clouds over the Arctic Ocean can be a challenge, consistent with previous studies [*Inoue et al.*,

2006; *Prenni et al.*, 2007]. Furthermore, the magnitudes of the sensible heat flux and surface heat transfer coefficient tend to be excessive. Sensitivity simulations suggest that the YSU PBL may improve the simulation of sensible heat flux over the MYJ scheme and lead to a significant reduction in a short-wave radiation bias during June 1998, but the sensitivity to the selection of the PBL scheme and the microphysics schemes otherwise tends to be small. A general improvement to the quality of the simulations, however, is not found by selection of alternative physics options in the sensitivity simulations. While the simulations demonstrate that there is still significant room for development and evaluation of physical parameterizations for polar applications, they do show that Polar WRF appears to be a highly capable tool for studies of Arctic Ocean meteorology. Further model development and testing is planned for Arctic land surfaces and Antarctic domains. This work should include a more general treatment of polar sea ice conditions.

Appendix A: Treatment of Arctic Sea-Ice Albedo

[45] Arctic sea ice has a strong seasonal cycle, with large changes not just in areal coverage, but also in critical surface characteristics [*Perovich et al.*, 2002b; *Persson et al.*, 2002]. *Perovich et al.* [2002a, 2007] demonstrate that surface albedo strongly depends on the seasonal freeze-thaw cycle. Unfortunately, a comprehensive specification of the variation is difficult as sea ice albedo varies between hemispheres and between thin seasonal sea ice and thicker multiyear ice. Some guidance on Southern Hemisphere sea ice albedo is available from *Wendler et al.* [2004], while *Perovich et al.* [2002a, 2002b, 2007] and *Persson et al.* [2002; also The surface energy budget during the onset of the melt season on the Arctic icepack during SHEBA, paper presented at 5th Conference on Polar Meteorology and Oceanography, American Meteorological Society, Dallas, Texas, 1999b] provide insight on multiyear Arctic sea ice. In this paper, we use a method designed for this research study in comparison to the SHEBA observations.

[46] *Perovich et al.* [2002a, 2007] present an idealized representation of the seasonal cycle with five stages: (1) a dry snow stage with a constant high albedo, (2) a melting snow stage with a gradual reduction in albedo, (3) a short melt pond formation period with a rapid decrease in albedo, (4) an extended melt pond evolution stage with a gradual reduction in albedo, and finally (5) a fall freezeup stage with the albedo trending upward toward values of the premelt season. Over the course of late spring and summer, albedo can decrease from values exceeding 0.8 to values half that magnitude. Summertime albedo can depend highly on the structure of melt ponds [*Perovich et al.*, 2002a, 2002b] and shows interannual variability associated with the freeze-thaw cycle [*Perovich et al.*, 2007]. Furthermore, the local albedo typically remains large, near 0.65, over bare ice [*Perovich et al.*, 2002a], and is near 0.07 over open ocean surfaces [*Pegau and Paulson*, 2001]. Thus, the partitioning of surface types is an important consideration for numerical modeling. To realistically capture the surface energy balance over the Arctic Ocean, therefore, we must attempt to capture the seasonal variability of the albedo, at least to the first order.

[47] In situ albedo measurements near SHEBA demonstrate sea-ice albedo is highly dependent on the seasonal cycle [*Perovich et al.*, 2002a, 2007; *Persson et al.*, 2002]. Figure 2 shows the time evolution of both the tower albedo at Ice Station SHEBA and the nearby transect albedo over summer 1998. From the lower-frequency variability in Figure 2, we can detect the transition from the "dry snow stage" to the beginning of summer conditions, initiated with a day of observed drizzle on 29 May [*Uttal et al.*, 2002; Persson et al., presented paper, 1999b]. The transect albedo is generally smaller than tower albedo during summer owing to the influence of melt ponds and leads on the former [e.g., *Persson et al.*, 2002]. Transect albedo shows a large decrease up until mid-June when widespread melt ponds were present. The albedo near SHEBA temporarily increased owing to wet snowfall near 19 June before decreasing again, and later reached a rough equilibrium in early July [*Perovich et al.*, 2002a]. Additional melting results in deeper and darker melt ponds as summer advances. The tower albedo later increases beginning about 12 August owing to refreezing [*Curry et al.*, 2001]. Snowfall over refrozen ponds assisted the albedo increase over the later half of August [*Perovich*, 2005].

[48] To provide insight into the seasonal rate of change that will influence the June simulation, Figure A1 shows surface broadband albedo derived from the Advanced Very High Resolution Radiometer (AVHRR) Advanced Polar Pathfinder (APP) [*Wang and Key*, 2005] data set as a function of latitude for 1 May, 16 May, 1 June, 16 June and 1 July 1998. The Extended AVHRR APP data sets are available from NSIDC [*Fowler et al.*, 2002]. The lower-latitude sea ice in the Pacific Ocean appears to have a smaller albedo than over the Arctic Ocean, and shows little time change in albedo magnitude. The AVHRR-derived albedo at SHEBA for June (not shown) agrees poorly with in situ measurements. Thus, the AVHRR values were judged to be inadequate for standalone input for sea-ice albedo. Nevertheless, the Arctic Ocean values in Figure A1 are useful to demonstrate a strong latitudinal dependence during early summer, in addition to the strong time dependence. Accordingly, summertime decrease in sea-ice albedo due to thaw occurs later at higher latitudes.

[49] Combining the time and latitudinal dependencies, we present an idealized model of the sea-ice albedo decrease over the Arctic Ocean during late spring and early summer. The time development is analogous to but simpler than the early summer stages of the *Perovich et al.* [2007] model. For the dry snow stage, we set the sea-ice albedo at 0.82, consistent with the maximum snow albedo in the parameterization of *Weatherly et al.* [1998]. Following the onset of the melt season, we linearly decrease sea-ice albedo over 35 days to a value of 0.5, the value of Weatherly et al. use for sea ice at 0°C. The 35-day decrease is based upon the observed trend at SHEBA from late May to early July (Figure 2). Melt ponds are treated as part of the sea-ice fraction and not the open water fraction, as early summer melt ponds frequently have a much higher albedo than open water. The June cycle of model surface albedo interpolated to SHEBA is displayed in Figure 2. Because the plotted field includes the influence of both ice and open water fractions, the Polar WRF value temporarily decreases on 22 June when an increased open water fraction was present.
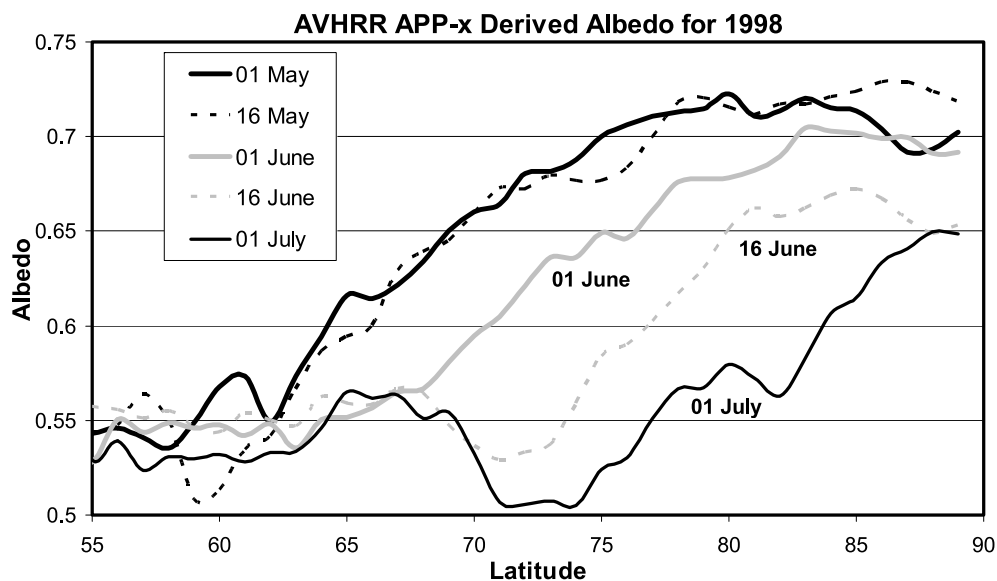
AVHRR APP-x Derived Albedo for 1998

Figure A1. Northern Hemisphere sea-ice albedo as a function of latitude derived from AVHRR APP observations for 1 May, 16 May, 1 June, 16 June, and 1 July 1998.

[50] To determine onset of the 35-day albedo decrease, the NSIDC snowmelt onset data set was applied. Estimated Julian date of snowmelt onset on sea ice is derived from SSM/I brightness temperatures [*Drobot and Anderson*, 2001]. Figure A2 shows the Julian onset date as a function of latitude within the model domain area. As expected, the onset date occurs later in the year proceeding northward. This relationship was applied for all latitudes of sea ice in the domain. Longitudinal variation of the onset date was not allowed for simplicity. From the values averaged over longitude within the domain, Figure A2 estimates a snowmelt onset in early June at the SHEBA site. Thus, this

procedure results in a slight lag at SHEBA for the albedo cycle during June in the Polar WRF simulation compared to the in situ observations. The lag contributes to the typically higher model albedo than transect albedo shown in Figure 2. In contrast, the tower albedo, measured primarily over ice, is generally greater than the Polar WRF albedo during June.

[51] For August, the summer development of the melt ponds has resulted in typically deeper and darker ponds than present during June. The average depth of the summer melt ponds near SHEBA eventually reached a maximum of 0.39 m [*Curry et al.*, 2001]. Therefore, a somewhat different methodology was employed for late summer albedo, when
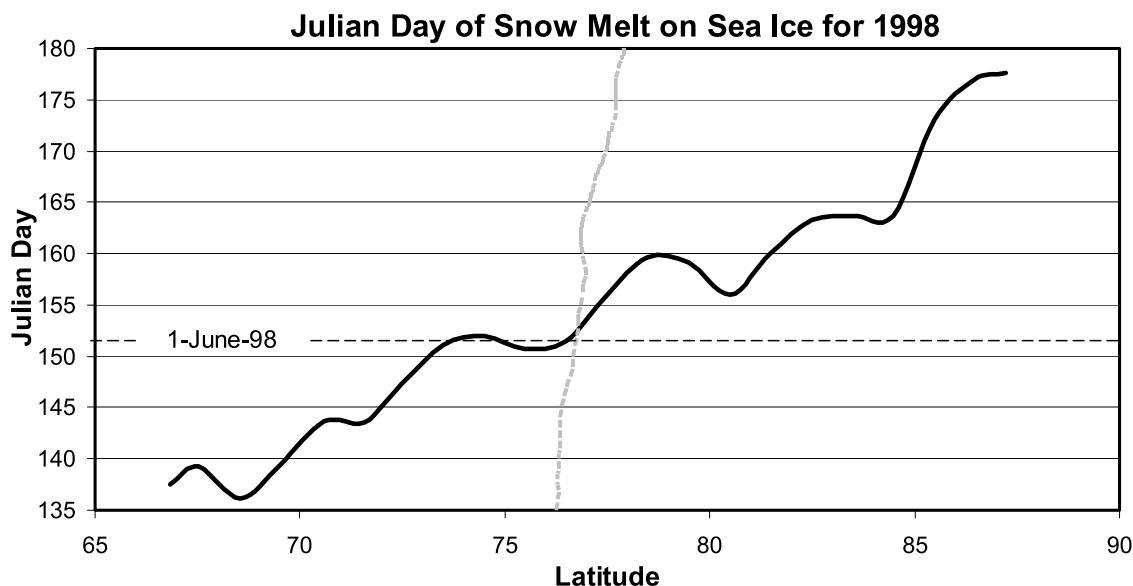
Julian Day of Snow Melt on Sea Ice for 1998

Figure A2. Julian day (thick solid line) for snowmelt on sea ice as a function of latitude for 1998. Melt date is from NSIDC SSM/I observations. Latitude of Ice Station SHEBA is show by the dashed gray line.

mature melt ponds can have an albedo similar to that of open water. Melt ponds are treated as open water, while the Noah LSM was only applied for the bare ice fraction of August sea-ice points. For this month, the open water fraction from SSM/I observation was much higher near SHEBA, and for the Arctic Ocean in general, than during June. The strong latitudinal dependence on Arctic Ocean albedo seen in Figure A1 for June was not found for August (not shown), so no latitudinal dependence of sea-ice albedo was included in the simulation of the late summer month. Figure 2 demonstrates an overall positive trend in observed albedo during the latter half of August, consistent with pond refreezing and snow accumulation [*Curry et al.*, 2001; *Perovich*, 2005]. We selected an albedo of 0.65 for bare ice up to 12 August, then a linear increase over time from 0.65 on 13 August to 0.82 on 1 September, more or less consistent with the trend for the tower albedo seen in Figure 2.

References

ACIA (2005), *Impacts of a Warming Climate: Arctic Climate Impact Assessment*, 140 pp., Cambridge Univ. Press, New York.

Avissar, R., and R. A. Pielke (1989), A parameterization of heterogeneous land surface for atmospheric numerical models and its impact on regional meteorology, *Mon. Weather Rev.*, 117, 2113–2136, doi:10.1175/1520-0493(1989)117<2113:APOHLS>2.0.CO;2.

Bromwich, D. H., and S.-H. Wang (2005), Evaluation of the NCEP/NCAR and ECMWF 15/40-yr reanalyses using rawinsonde data from two independent Arctic field experiments, *Mon. Weather Rev.*, 133, 3562–3578, doi:10.1175/MWR3043.1.

Bromwich, D. H., J. J. Cassano, T. Klein, G. Heinemann, K. M. Hines, K. Steffen, and J. E. Box (2001), Mesoscale modeling of katabatic winds over Greenland with the Polar MM5, *Mon. Weather Rev.*, 129, 2290–2309, doi:10.1175/1520-0493(2001)129<2290:MMOKWO>2.0.CO;2.

Bromwich, D. H., A. J. Monaghan, J. J. Powers, J. J. Cassano, H. Wei, Y. Kuo, and A. Pellegrini (2003), Antarctic Mesoscale Prediction System (AMPS): A case study from the 2000/2001 field season, *Mon. Weather Rev.*, 131, 412–434, doi:10.1175/1520-0493(2003)131<0412:AMPSAA>2.0.CO;2.

Bromwich, D. H., L.-S. Bai, and G. G. Bjarnason (2005a), High resolution regional climate simulations over Iceland using Polar MM5: 1991–2000, *Mon. Weather Rev.*, 133, 3527–3547, doi:10.1175/MWR3049.1.

Bromwich, D. H., E. R. Toracinta, R. J. Oglesby, J. L. Fastook, and T. J. Hughes (2005b), LGM summer climate on the southern margin of the Laurentide Ice Sheet: Wet or dry?, *J. Clim.*, 18, 3317–3338, doi:10.1175/JCLI3480.1.

Bromwich, D. H., R. L. Fogt, K. E. Hodges, and J. E. Walsh (2007), A tropospheric assessment of the ERA-40, NCEP, and JRA-25 global reanalyses in the polar regions, *J. Geophys. Res.*, 112, D10111, doi:10.1029/2006JD007859.

Cassano, J. J., J. E. Box, D. H. Bromwich, L. Li, and K. Steffen (2001), Evaluation of Polar MM5 simulations of Greenland's atmospheric circulation, *J. Geophys. Res.*, 106, 33,867–33,889, doi:10.1029/2001JD900044.

Chen, F., and J. Dudhia (2001), Coupling an advanced land-surface/hydrology model with the Penn State/NCAR MM5 modeling system. Part I: Model description and implementation, *Mon. Weather Rev.*, 129, 569–585, doi:10.1175/1520-0493(2001)129<0569:CAALSH>2.0.CO;2.

Chou, M.-D., and M. J. Suarez (1999), A solar radiation parameterization for atmospheric studies, *NASA Tech. Rep. NASA/TM-1999–10460*, 15, 38 pp., NASA Goddard Space Flight Cent., Greenbelt. Md. (Available at http://ntrs.nasa.gov/)

Comiso, J. (2002), Bootstrap sea ice concentrations for NIMBUS-7 SMMR and DMSP SSM/I, June to September 2001, http://nsidc.org/data/nsidc-0079.html, Natl. Snow and Ice Data Cent, Boulder, Colo.

Cucurull, L., Y. Kuo, D. M. Barker, and S. R. H. Rizvi (2006), Assessing the impact of COSMIC GPS radio occultation data on weather analysis and short-term forecasts over the Antarctic, *Mon. Weather Rev.*, 134, 3283–3296, doi:10.1175/MWR3241.1.

Curry, J. A. (2001), Introduction to special section: FIRE Arctic Clouds Experiment, *J. Geophys. Res.*, 106, 14,985–14,987, doi:10.1029/2000JD900551.

Curry, J. A., and A. M. Lynch (2002), Comparing Arctic regional climate models, *Eos Trans. AGU*, 83, 87, doi:10.1029/2002EO000051.

Curry, J. A., et al. (2000), FIRE Arctic Clouds Experiment, *Bull. Am. Meteorol. Soc.*, 81, 5–29, doi:10.1175/1520-0477(2000)081<0005:FACE>2.3.CO;2.

Curry, J. A., J. L. Schramm, D. K. Perovich, and J. O. Pinto (2001), Applications of SHEBA/FIRE data to evaluation of snow/ice albedo parameterizations, *J. Geophys. Res.*, 106, 15,345–15,355, doi:10.1029/2000JD900311.

DeWeaver, E., and C. M. Bitz (2006), Atmospheric circulation and Arctic sea ice in CCSM3 at medium and high resolution, *J. Clim.*, 19, 2415–2436, doi:10.1175/JCLI3753.1.

Drobot, S., and M. Anderson (2001), Comparison of interannual snowmelt onset dates with atmospheric conditions, *Ann. Glaciol.*, 33, 79–84, doi:10.3189/172756401781818851.

Ebert, E., and J. A. Curry (1993), An intermediate one-dimensional thermodynamic sea ice model for investigating ice-atmosphere interactions, *J. Geophys. Res.*, 98, 10,085–10,109, doi:10.1029/93JC00656.

Fowler, C., J. Maslanik, T. Haran, T. Scambos, J. Key, and W. Emery (2002), AVHRR Polar Pathfinder twice-daily 25 km EASE-Grid composites, http://www.nsidc.org/data/nsidc-0066.html, Natl. Snow and Ice Data Cent., Boulder, Colo.

Grachev, A., C. Fairall, P. Persson, E. Andreas, and P. Guest (2005), Stable boundary-layer scaling regimes: The SHEBA data, *Boundary Layer Meteorol.*, 116, 201–235, doi:10.1007/s10546-004-2729-0.

Grell, G. A., and D. Devenyi (2002), A generalized approach to parameterizing convection combining ensemble and data assimilation techniques, *Geophys. Res. Lett.*, 29(14), 1693, doi:10.1029/2002GL015311.

Grell, G. A., J. Dudhia, and D. R. Stauffer (1994), A description of the fifth-generation Penn State/NCAR mesoscale model (MM5), *NCAR Tech. Note NCAR/TN3981+STR*, 122 pp., Natl. Cent. for Atmos. Res., Boulder, Colo.

Guo, Z., D. H. Bromwich, and J. J. Cassano (2003), Evaluation of Polar MM5 simulations of Antarctic atmospheric circulation, *Mon. Weather Rev.*, 131, 384–411, doi:10.1175/1520-0493(2003)131<0384:EOPMSO>2.0.CO;2.

Hines, K. M., and D. H. Bromwich (2008), Development and testing of Polar WRF. Part I: Greenland Ice Sheet meteorology, *Mon. Weather Rev.*, 136, 1971–1989, doi:10.1175/2007MWR2112.1.

Hong, S.-Y., J. Dudhia, and S.-H. Chen (2004), A revised approach to ice microphysical processes for the bulk parameterization of clouds and precipitation, *Mon. Weather Rev.*, 132, 103–120, doi:10.1175/1520-0493(2004)132<0103:ARATIM>2.0.CO;2.

Hong, S.-Y., Y. Noh, and J. Dudhia (2006), A new vertical diffusion package with an explicit treatment of entrainment processes, *Mon. Weather Rev.*, 134, 2318–2341, doi:10.1175/MWR3199.1.

Huwald, H., L.-B. Tremblay, and H. Blatter (2005), A multilayer sigma-coordinate thermodynamic sea ice model: Validation against Surface Heat Budget of the Arctic Ocean (SHEBA)/Sea Ice Model Intercomparison Project Part 2 (SIMIP2) data, *J. Geophys. Res.*, 110, C05010, doi:10.1029/2004JC002328.

Inoue, J., J. Liu, J. O. Pinto, and J. A. Curry (2006), Intercomparison of Arctic regional climate models: Modeling clouds and radiation for SHEBA in May 1998, *J. Clim.*, 19, 4167–4178, doi:10.1175/JCLI3854.1.

Janjić, Z. I. (2002), Nonsingular implementation of the Mellor–Yamada level 2.5 scheme in the NCEP Meso model, *NCEP Off. Note 437*, 61 pp., Natl. Cent. For Environ. Prot., Camp Springs, Md.

Lüpkes, C., T. Vihma, G. Birnbaum, and U. Wacker (2008), Influence of leads in sea ice on the temperature of the atmospheric boundary layer during polar night, *Geophys. Res. Lett.*, 35, L03805, doi:10.1029/2007GL032461.

Mahrt, L., and D. Vickers (2005), Moisture fluxes over snow with and without protruding vegetation, *Q. J. R. Meteorol. Soc.*, 131, 1251–1270, doi:10.1256/qj.04.66.

McBean, G., G. Alekseev, D. Chen, E. Førland, J. Fyfe, P. Y. Groisman, R. King, H. Melling, R. Vose, and P. H. Whitfield (2004), Arctic climate: Past and present, in *Arctic Climate Impact Assessment*, pp. 21–60, Cambridge Univ. Press, New York.

Mlawer, E. J., S. J. Taubman, P. D. Brown, M. J. Iacono, and S. A. Clough (1997), Radiative transfer for inhomogeneous atmosphere: RRTM, a validated correlated-k model for the longwave, *J. Geophys. Res.*, 102, 16,663–16,682, doi:10.1029/97JD00237.

Monaghan, A. J., D. H. Bromwich, J. G. Powers, and K. W. Manning (2005), The climate of the McMurdo, Antarctica region as represented

by one year of forecasts from the Antarctic Mesoscale Prediction System, *J. Clim.*, *18*, 1174–1189, doi:10.1175/JCLI3336.1.

Morrison, H., and J. O. Pinto (2005), Mesoscale modeling of springtime arctic mixed-phase stratiform clouds using a new two-moment bulk microphysics scheme, *J. Atmos. Sci.*, *62*, 3683–3704, doi:10.1175/JAS3564.1.

Morrison, H., and J. O. Pinto (2006), Intercomparison of bulk cloud microphysics schemes in mesoscale simulations of springtime arctic mixed-phase stratiform clouds, *Mon. Weather Rev.*, *134*, 1880–1900, doi:10.1175/MWR3154.1.

Morrison, H., J. A. Curry, and V. I. Khvorostyanov (2005), A new double-moment microphysics parameterization for application in cloud and climate models. Part I: Description, *J. Atmos. Sci.*, *62*, 1665–1677, doi:10.1175/JAS3446.1.

Morrison, H., J. O. Pinto, J. A. Curry, and G. M. McFarquhar (2008), Sensitivity of arctic mixed-phase stratocumulus to cloud condensation and ice nuclei over regionally varying surface conditions, *J. Geophys. Res.*, *113*, D05203, doi:10.1029/2007JD008729.

Overland, J. E., S. L. McNutt, J. Groves, S. Salo, E. L. Andreas, and P. O. G. Persson (2000), Regional sensible and radiative heat flux estimates for the winter Arctic during the Surface Heat Budget of the Arctic Ocean (SHEBA) experiment, *J. Geophys. Res.*, *105*, 14,093–14,102, doi:10.1029/1999JC000010.

Overland, J., J. Calder, F. Fetterer, D. McGuire, J. Morison, J. Richter-Menge, N. Soriede, and J. Walsh (2003), SEARCH workshop on large-scale atmosphere/cryosphere observations, *Bull. Am. Meteorol. Soc.*, *84*, 1077–1082, doi:10.1175/BAMS-84-8-1077.

Parish, T. R. (1984), A numerical study of strong katabatic winds over Antarctica, *Mon. Weather Rev.*, *112*, 545–554, doi:10.1175/1520-0493(1984)112<0545:ANSOSK>2.0.CO;2.

Pegau, W. S., and C. A. Paulson (2001), The albedo of Arctic leads in summer, *Ann. Glaciol.*, *33*, 221–224, doi:10.3189/172756401781818833.

Perovich, D. K. (2005), On the aggregate-scale partitioning of solar radiation in Arctic sea ice during the Surface Heat Budget of the Arctic Ocean (SHEBA) field experiment, *J. Geophys. Res.*, *110*, C03002, doi:10.1029/2004JC002512.

Perovich, D. K., et al. (1999), Year on ice gives climate insights, *Eos Trans. AGU*, *80*(41), 481, 485–486.

Perovich, D. K., T. C. Grenfell, B. Light, and P. V. Hobbs (2002a), Seasonal evolution of Arctic sea ice albedo, *J. Geophys. Res.*, *107*(C10), 8044, doi:10.1029/2000JC000438.

Perovich, D. K., W. B. Tucker III, and K. A. Ligett (2002b), Aerial observations of the evolution of ice surface conditions during summer, *J. Geophys. Res.*, *107*(C10), 8048, doi:10.1029/2000JC000449.

Perovich, D. K., S. V. Nghiem, T. Markus, and A. Schweiger (2007), Seasonal evolution and interannual variability of the local solar energy absorbed by the Arctic sea ice–ocean system, *J. Geophys. Res.*, *112*, C03005, doi:10.1029/2006JC003558.

Persson, P. O. G., C. W. Fairall, E. L. Andreas, P. S. Guest, and D. K. Perovich (2002), Measurements near the Atmospheric Surface Flux Group Tower at SHEBA: Near-surface conditions and surface energy budget, *J. Geophys. Res.*, *107*(C10), 8045, doi:10.1029/2000JC000705.

Pinto, J. O., J. A. Curry, and C. W. Fairall (1997), Radiative characteristics of the Arctic atmosphere during spring as inferred from ground-based measurements, *J. Geophys. Res.*, *102*, 6941–6952, doi:10.1029/96JD03348.

Powers, J. G. (2007), Numerical prediction of an Antarctic severe wind event with the weather research and forecasting (WRF) model, *Mon. Weather Rev.*, *135*, 3134–3157, doi:10.1175/MWR3459.1.

Powers, J. G., A. J. Monaghan, A. M. Cayette, D. H. Bromwich, Y.-H. Kuo, and K. W. Manning (2003), Real-time mesoscale modeling over Antarctica: The Antarctic Mesoscale Prediction System (AMPS), *Bull. Am. Meteorol. Soc.*, *84*, 1533–1545, doi:10.1175/BAMS-84-11-1533.

Prenni, A. J., J. Y. Harrington, M. Tjernström, P. J. DeMott, A. Avramov, C. N. Long, S. M. Kreidenweis, P. Q. Olsson, and J. Verlinde (2007), Can ice-nucleating aerosols affect Arctic seasonal climate?, *Bull. Am. Meteorol. Soc.*, *88*, 541–550, doi:10.1175/BAMS-88-4-541.

Shupe, M. D., and J. M. Intrieri (2004), Cloud radiative forcing of the Arctic surface: The influence of clouds properties, surface albedo, and solar zenith angle, *J. Clim.*, *17*, 616–628, doi:10.1175/1520-0442(2004)017<0616:CRFOTA>2.0.CO;2.

Shupe, M. D., T. Uttal, and S. Y. Matrosov (2005), Arctic cloud microphysics retrievals from surface-based remote sensors at SHEBA, *J. Appl. Meteorol.*, *44*, 1544–1562, doi:10.1175/JAM2297.1.

Skamarock, W. C., J. B. Klemp, J. Dudhia, D. O. Gill, D. M. Barker, W. Wang, and J. G. Powers (2005), A description of the advanced research WRF version 2, *NCAR Tech. Note NCAR/TN–468+STR*, 88 pp., Natl. Cent. for Atmos. Res., Boulder, Colo.

Stroeve, J. C., J. E. Box, C. Fowler, T. Haran, and J. Key (2001), Intercomparison between in situ and AVHRR Polar Pathfinder-derived surface albedo over Greenland, *Remote Sens. Environ.*, *75*, 360–374, doi:10.1016/S0034-4257(00)00179-6.

Stroeve, J., M. M. Holland, W. Meier, T. Scambos, and M. Serreze (2007), Arctic sea ice decline: Faster than forecast, *Geophys. Res. Lett.*, *34*, L09501, doi:10.1029/2007GL029703.

Thompson, G., R. M. Rasmussen, and K. Manning (2004), Explicit forecasts of winter precipitation using an improved bulk microphysics scheme. Part I: Description and sensitivity analysis, *Mon. Weather Rev.*, *132*, 519–542, doi:10.1175/1520-0493(2004)132<0519:EFOWPU>2.0.CO;2.

Tjernström, M., M. Zagar, G. Svensson, J. Cassano, S. Pfeifer, A. Rinke, K. Wyser, K. Dethloff, C. Jones, and T. Semmler (2005), Modelling the Arctic boundary layer: An evaluation of six ARCMIP regional-scale models with data from the SHEBA project, *Boundary Layer Meteorol.*, *117*, 337–381, doi:10.1007/s10546-004-7954-z.

Uppala, S. M., et al. (2005), The ERA-40 re-analysis, *Q. J. R. Meteorol. Soc.*, *131*, 2961–3012, doi:10.1256/qj.04.176.

Uttal, T., et al. (2002), Surface Heat Budget of the Arctic Ocean, *Bull. Am. Meteorol. Soc.*, *83*, 255–275, doi:10.1175/1520-0477(2002)083<0255:SHBOTA>2.3.CO;2.

Valkonen, T., T. Vihma, and M. Doble (2008), Mesoscale modeling of the atmosphere over Antarctic sea ice: A late-autumn case study, *Mon. Weather Rev.*, *136*, 1457–1474, doi:10.1175/2007MWR2242.1.

Verlinde, J., et al. (2007), The mixed-phase Arctic cloud experiment, *Bull. Am. Meteorol. Soc.*, *88*, 205–221, doi:10.1175/BAMS-88-2-205.

Vihma, T. (1995), Subgrid parameterization of surface heat and momentum fluxes over polar oceans, *J. Geophys. Res.*, *100*, 22,625–22,646.

Wang, X., and J. R. Key (2005), Arctic surface, cloud, and radiation properties based on the AVHRR Polar Pathfinder dataset. Part I: Spatial and temporal characteristics, *J. Clim.*, *18*, 2558–2574, doi:10.1175/JCLI3438.1.

Weatherly, J. W., B. P. Briegleb, W. G. Large, and J. A. Maslanik (1998), Sea ice and polar climate of the NCAR CSM, *J. Clim.*, *11*, 1472–1486, doi:10.1175/1520-0442(1998)011<1472:SIAPCI>2.0.CO;2.

Wendler, G., B. Moore, B. Hartmann, M. Stuefer, and R. Flint (2004), Effects of multiple reflection and albedo on the net radiation in the pack ice zones of Antarctica, *J. Geophys. Res.*, *109*, D06113, doi:10.1029/2003JD003927.

Xiao, Q., Y.-H. Kuo, Z. Ma, W. Huang, X.-Y. Huang, X. Zhang, D. M. Barker, J. Michalakes, and J. Dudhia (2008), Application of an adiabatic WRF adjoint to the investigation of the May 2004 McMurdoAntarctica, severe wind event, Mon., *Weather Rev.*, *136*, 3696–3713, doi:10.1175/2008MWR2235.1.

Zhang, J., and D. A. Rothrock (2005), Effect of sea ice rheology in numerical investigations of climate, *J. Geophys. Res.*, *110*, C08014, doi:10.1029/2004JC002599.

_____

L.-S. Bai, D. H. Bromwich, and K. M. Hines, Polar Meteorology Group, Byrd Polar Research Center, Ohio State University, 1090 Carmack Road, Columbus, OH 43210-1002, USA. (hines.91@osu.edu)